

Magnetized Accretion and Dead Zones in Protostellar Disks

Natalia Dzyurkevich^{1,2}, Neal J. Turner³, Thomas Henning¹, Wilhelm Kley⁴

¹*Max Planck Institute for Astronomy, Königstuhl 17, 69117 Heidelberg, Germany*

²*Laboratoire de radioastronomie, UMR 8112 du CNRS, Ecole Normale Supérieure et Observatoire de Paris, 24 rue de Lhomond, 75231, Paris Cedex 05, France*

³*Jet Propulsion Laboratory, California Institute of Technology, Pasadena, California 91109, USA*

⁴*University of Tübingen, Auf der Morgenstelle 10, Tübingen, 72076 Germany*

ABSTRACT

The edges of magnetically-dead zones in protostellar disks have been proposed as locations where density bumps may arise, trapping planetesimals and helping form planets. Magneto-rotational turbulence in magnetically-active zones provides both accretion of gas on the star and transport of mass to the dead zone. We investigate the location of the magnetically-active regions in a protostellar disk around a solar-type star, varying the disk temperature, surface density profile, and dust-to-gas ratio. We also consider stellar masses between 0.4 and 2 M_{\odot} , with corresponding adjustments in the disk mass and temperature. The dead zone's size and shape are found using the Elsasser number criterion with conductivities including the contributions from ions, electrons, and charged fractal dust aggregates. The charged species' abundances are found using the approach proposed by Okuzumi. The dead zone is in most cases defined by the ambipolar diffusion. In our maps, the dead zone takes a variety of shapes, including a fish-tail pointing away from the star and islands located on and off the midplane. The corresponding accretion rates vary with radius, indicating locations where the surface density will increase over time, and others where it will decrease. We show that density bumps do not readily grow near the dead zone's outer edge, independently of the disk parameters and the dust properties. Instead, the accretion rate peaks at the radius where the gas-phase metals freeze out. This could lead to clearing a valley in the surface density, and to a trap for pebbles located just outside the metal freeze-out line.

1. Introduction

Trapping solid material is a basic requirement for forming planets enriched in the heavy elements with respect to the central star. One way to trap solid particles is through gas pressure gradients. If the pressure locally increases with distance from the star, radial force balance dictates the gas orbit faster than Keplerian. Embedded particles then feel a tailwind, receive orbital angular momentum from the gas, and drift away from the star, collecting near the point where the general outward pressure decline resumes. Such local radial pressure maxima can occur in various ways.

They can form at the distance where the disk’s main heat source switches from accretion power to stellar illumination (Hasegawa & Pudritz 2010b,a, 2011), or can be part of long-lived zonal flows (Johansen et al. 2009; Uribe et al. 2011; Pinilla et al. 2012). Pressure bumps can also be made by unsteadiness in the overall inward spiraling of the disk gas that feeds the growth of the central star. Material will pile up where the inflow becomes slower than average.

The best candidate to drive the disk’s inflow is turbulence driven by the magneto-rotational instability or MRI (Balbus & Hawley 1991; Hawley et al. 1995; Balbus & Hawley 1998). Since the MRI relies on magnetic forces, the disk gas must be ionized enough to couple to the fields. The low temperatures rule out thermal ionization, but the disk surface layers are nevertheless partly ionized because they absorb X-rays from the young star and cosmic rays from interstellar space (Gammie 1996; Glassgold et al. 1997). The ionization is balanced by recombination on dust grains in the disk interior (Sano et al. 2000), so that the grains’ abundance regulates the flow of material through the disk.

Time-unsteady flow leading to local pressure maxima can occur where the disk crosses the threshold from magnetically-coupled to decoupled, at the dead zones’ inner and outer radial edges (Lyra et al. 2009; Dzyurkevich et al. 2010). Away from the edges, pressure bumps could arise from changes in the rate of flow through the magnetically-active surface layers above and below the dead zone. Such interruptions in the layered flow might come from a jump in the dust recombination cross-section across the snow line (Kretke & Lin 2007; Brauer et al. 2008).

The dead zone itself can participate in the overall radial flow. Even where the resistivity is high enough to damp away the MRI, and magnetic forces cannot directly drive turbulence, the stresses can be non-zero due to waves propagating from nearby turbulent regions (Fleming & Stone 2003; Dzyurkevich et al. 2010; Okuzumi & Hirose 2011) and to hydrodynamical instabilities and gas-particle interaction (Weidenschilling & Cuzzi 1993; Johansen & Youdin 2007; Johansen et al. 2011). The dead zone stresses affect the timescales for material to pile up in orbit around the star, and so must be considered when attempting to use the time-evolving flow in layered disks to explain episodic accretion events such as FU Orionis outbursts (Armitage et al. 2001; Martin et al. 2012; Martin & Livio 2012; Zhu et al. 2010).

The size and shape of the dead zone thus govern many aspects of protostellar disks’ evolution. The dead zone’s edges are determined by the non-ideal terms in the induction equation corresponding to Ohmic, Hall and ambipolar diffusion. The Ohmic term is typically strongest in the dense disk interior, the Hall term at intermediate densities and the ambipolar term in the disk’s low-density atmosphere and outer reaches (Wardle & Ng 1999; Wardle 2007; Sano & Stone 2002a; Perez-Becker & Chiang 2011).

The dead zone determined by the Ohmic diffusivity has been mapped under ionization by cosmic rays (Sano et al. 2000), X-rays (Ilgner & Nelson 2006) and stellar energetic protons (Turner & Drake 2009). Recently its extent was estimated with a more precise magnetic field distribution using a sequence of local shearing-box chemical-MHD calculations (Flaig et al. 2012). The impact of the

Ohmic diffusion might be reduced by the associated magnetic dissipation heating, at least near the star where temperatures approach the thermal ionization threshold (Muranushi et al. 2012).

The Hall term has at most a weak effect on the saturated strength of the MRI turbulence, at least when the Hall and Ohmic terms are not too different in magnitude, according to numerical calculations (Sano & Stone 2002b). Wardle & Salmeron (2012) however suggest that the results would differ at very large ratios of Hall to the other terms. When the Hall term is taken into account in this regime, the gas flow through the magnetically-active layers could be faster.

Ambipolar diffusion becomes important when collisions are rare enough that the neutral gas drifts with respect to the plasma. Analysis of the MRI in the linear regime (Blaes & Balbus 1994; Kunz & Balbus 2004; Desch 2004) shows that the instability is suppressed when the plasma transfers its momentum to the neutrals slower than the instability grows. The non-linear evolution of the MRI was first modeled by Mac Low et al. (1995) in two spatial dimensions, followed by Brandenburg et al. (1995) for the strong coupling regime. In 3-D two-fluid local-box simulations the non-linear MRI under ambipolar diffusion was studied by Hawley & Stone (1998) for several different magnetic field configurations. Bai (2011) show that the turbulent accretion stress declines smoothly with increasing ambipolar diffusivity, from around 1% of the gas pressure at the threshold for MRI turbulence down to 7×10^{-4} at diffusivities ten times greater. The local shearing-box simulations were unstratified. In Simon et al. (2012), MRI turbulence on azimuthal background magnetic fields was modeled for conditions similar to those thought to occur in the outer reaches of protostellar disks. The turbulence died out almost completely below the threshold ambipolar diffusivity.

The ionization degree of the gas is affected by the dust surface area available to sweep up the ions and electrons. The recombination cross-section is often treated as residing on compact spherical grains (Semenov et al. 2004; Ilgner & Nelson 2006; Turner & Sano 2008; Turner et al. 2010) so that the area decreases as the grains grow. Here we take the alternative approach of Okuzumi (2009), supposing that at least the smaller grains bearing most of the cross-section remain as loose, fluffy aggregates of smaller particles. The fractal dimension is close to two and so the area remains unchanged as the aggregates grow. Larger particles may be compacted by collisions or internal forces as the solid material evolves toward planet formation, but we assume the small fluffy aggregates continue to dominate the recombination cross-section. Like Okuzumi we neglect the electrical polarization that affects small compact grains’ interaction with approaching charges, and compute the abundances of the ions and electrons, and the charge state distribution of the aggregates, from his governing equation (his eq. 30).

The situation with the magnetic diffusivity is complicated by the fact that the grains carry charge. Small PAH-like particles, due to their low mass and relatively high cyclotron frequencies, can significantly change the disk’s overall magnetic coupling (Bai 2011; Perez-Becker & Chiang 2011) (Mohanty, Ercolano & Turner, in press). More-massive compact grains have little direct effect on the electrical current because of their low cyclotron frequencies, even when charged to the

limit where further electrons are repelled by the electrostatic force Wardle (2007). Fluffy aggregates however, due to their large surface area, can accommodate many more elementary charges. We therefore include the aggregates’ contributions to the conductivities.

In this paper we study the factors determining the dead zone’s extent in the presence of fluffy grains. After presenting a fiducial model we vary the size of the monomers making up the fluffy aggregates, the aggregates’ abundance relative to the gas, the overall disk mass and the surface density power-law index, the gas temperature, the stellar mass and the strength of the cosmic ray ionization. Across this parameter space we find the magnetically-dead region has a diversity of shapes and sizes.

The paper is laid out as follows. In section 2 we describe how we calculate the ionization state. Section 3 has an outline of the magnetic dissipation mechanisms and the criteria for coupling the gas to the magnetic field. In section 4 we present the resulting dead zone shape as a function of the monomer size, dust-to-gas ratio and other parameters. We discuss the implications for building local pressure maxima in section 5, and summarize our findings in section 6.

2. Fiducial Disk Model

2.1. Gas and magnetic field

We begin by mapping the dead zone in a fiducial disk model, taking stellar mass $M_* = 1M_\odot$ and normalizing the surface density to $\Sigma = 1700 \text{ gcm}^{-2}$ and the temperature to $T = 280 \text{ K}$, both at 1 AU. Rather than a power-law surface density profile, we use a power-law with exponential outer roll-off, the similarity solution obtained by Hartmann et al. (1998). This profile yields a good match between the radii of the disk measured in CO emission and in dust continuum Hughes et al. (2008). The surface density falls off with the radius r as

$$\Sigma = \Sigma_c \left(\frac{r}{r_c}\right)^{-p} \exp\left[-\left(\frac{r}{r_c}\right)^{2-p}\right], \quad (1)$$

where Σ_c , the surface density at the cut-off radius r_c , is equal to

$$\Sigma_c = (2 - p) \frac{M_{\text{disk}}}{2\pi r_c^2}. \quad (2)$$

We take the median power-law index $p = 0.9$ observed by Andrews et al. (2009) in the Ophiuchus star-forming region, and set the cut-off radius r_c to 40 AU. The surface density then matches the standard minimum-mass Solar nebula at 1 AU and again at 100 AU. The disk’s whole mass of $M_{\text{disk}} = 0.064M_\odot$ is stable against self-gravity, as the Toomre parameter is nowhere lower than 4. The density is easily reconstructed as

$$\rho = \frac{\Sigma}{\sqrt{2\pi} c_0 r \sin(\Theta)} \cdot \exp\left(-\frac{\cos \Theta^2}{2c_0^2 \sin \Theta^2}\right), \quad (3)$$

where $R = r \sin(\Theta)$ is the cylindrical radius and $c_0 = H/(r \sin \Theta)$ the isothermal sound speed, with H the pressure scale height. Here we use spherical coordinates (r, Θ, ϕ) with the rotation axis corresponding to $\Theta = 0$. The orbital angular speed and temperature are

$$\Omega = \sqrt{\frac{GM_*}{(r \sin \Theta)^3}} \quad \text{and} \quad T = T_0 \sqrt{\frac{r_{\text{in}}}{r \sin \Theta}}, \quad (4)$$

with $T_0 = 280$ K at $r_{\text{in}} = 1$ AU. The surface density profile with and without the exponential roll-off is shown in Fig. 1. Cosmic rays reach the midplane largely unimpeded at $r > 15$ AU. Scattered X-rays similarly reach the midplane outside $r > 60$ AU. Nevertheless, the thin gas in the outer disk could be magneto-rotationally stable due to ambipolar diffusion. To map any stable regions, we need to obtain the densities of the charged species in a multi-component plasma.

We calculate the conductivities in the domain extending from 1 to 200 AU in radius and over $\pi/2 \pm 0.4$ in the polar angle Θ . The disk’s concave or flaring shape means the model covers ± 12 pressure scale heights at 1 AU but just $\pm 5H$ at 200 AU.

We give the disk a mean vertical magnetic field,

$$B = \sqrt{8\pi \hat{\rho} \hat{c}_s^2 / \beta_{p,0}}, \quad (5)$$

where the midplane plasma beta $\beta_{p,0} = 400$ is a constant and $\hat{\rho}(r)$ and $\hat{c}_s(r)$ are the gas density and sound speed at the midplane. The RMS vertical magnetic field in the saturated MRI turbulence varies only slightly with height up to the location where the plasma beta falls below unity, in stratified local ideal-MHD shearing-box calculations by Miller & Stone (2000). To simplify matters we therefore make the field strength independent of height.

2.2. Dust

We assume a two-component dust population consisting of fractal porous aggregates and larger, more compact rocks. The fluffy aggregates couple well to the gas through drag forces (Meakin 1991; Blum 2004; Dominik et al. 2007) and we assume they remain well-mixed in the gas, with dust-to-gas mass ratio f_{dg} . Both numerical (Kempf et al. 1999) and experimental studies (Wurm & Blum 1998; Blum et al. 1998; Blum & Wurm 2000) show that such aggregates form at early growth stages when grain-grain collisions are slow. The outcome is an ensemble of fractal aggregates with fractal dimension $D \leq 2$, with a narrow, quasi-monodisperse mass distribution. The fractal growth continues until the aggregates reach centimeter sizes (Suyama et al. 2008). The compact bodies in contrast have $D \sim 3$. They may form in low-probability collisions between the fluffy particles, with impact speeds high enough to modify the aggregates’ structure but too low for complete disruption.

The fluffy aggregates dominate the total cross-section for ions and electrons because of their much greater surface area per unit solid mass. The compact particles simply serve as a sink of solid material. The fluffy grains therefore determine the ionization state, even though the compact particles may contain most of the mass.

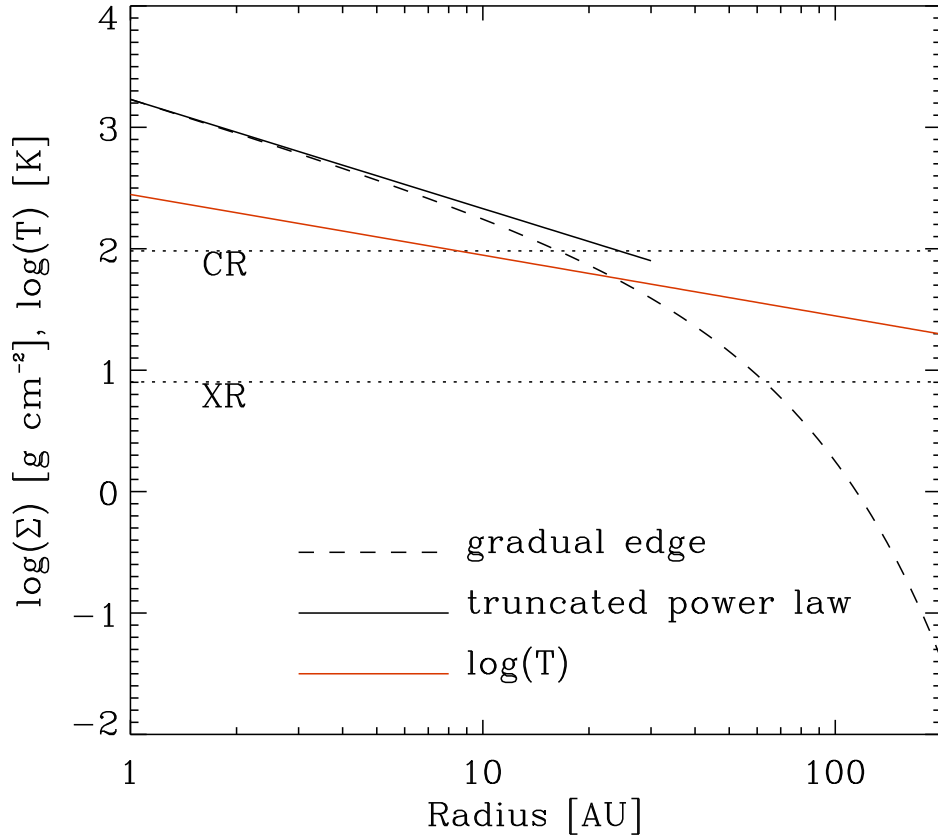


Fig. 1.— Surface density and temperature profiles in the fiducial model disk. The dashed line shows the surface density power law with exponential roll-off. The solid black line shows the power-law alone, while dotted gray lines indicate the penetration depths of cosmic rays and X-rays, 96 g cm^{-2} and 8 g cm^{-2} , respectively. The red line is the temperature profile.

2.3. Ionization and Recombination

Thermal ionization is effective only within less than 1 AU of the central star, where temperatures above 1 000 K mean alkali metals can ionize when colliding with hydrogen or helium (Umebayashi 1983). At the lower temperatures found further out, ionization comes from cosmic rays, stellar X-rays and ultraviolet photons, and radionuclides. Our model includes all these except the ultraviolet photons, which penetrate a mass column less than 0.1 g cm^{-2} (Perez-Becker & Chiang 2011) so we do not consider them further.

Most ionizations are of the abundant species, H_2 and helium. In the total ionization rate

$$\zeta = \zeta_{XR} + \zeta_{CR} + \zeta_{RN} \quad (6)$$

the cosmic ray contribution is

$$\zeta_{CR} = \frac{\zeta_{CR}^0}{2} \times \left[\exp\left(-\frac{D_a}{D_{CR}}\right) \left\{ 1 + \left(\frac{D_a}{D_{CR}}\right)^{3/4} \right\}^{-4/3} + \exp\left(-\frac{D_b}{D_{CR}}\right) \left\{ 1 + \left(\frac{D_b}{D_{CR}}\right)^{3/4} \right\}^{-4/3} \right]. \quad (7)$$

where the cosmic ray penetration depth $D_{CR} = 96 \text{ g cm}^{-2}$, and the mass column vertically above and below the point of interest are D_a and D_b respectively (Umebayashi & Nakano 2009). The cosmic ray ionization rate in the interstellar medium varies from 10^{-18} s^{-1} to 10^{-15} s^{-1} (Umebayashi & Nakano 1981; McCall et al. 2003a). As a fiducial value we choose $\zeta_{CR0} = 5 \times 10^{-18} \text{ s}^{-1}$.

The X-ray contribution to the ionization rate is

$$\zeta_{XR} = \frac{L_X}{10^{29} \text{ erg s}^{-1}} \left(\frac{1 \text{ AU}}{R}\right)^{2.2} \times \left(\zeta_1 \left[e^{-(N_{H1}/N_1)^{0.4}} + e^{-(N_{H2}/N_1)^{0.4}} \right] + \zeta_2 \left[e^{-(N_{H1}/N_2)^{0.65}} + e^{-(N_{H2}/N_2)^{0.65}} \right] \right), \quad (8)$$

where the direct X-rays' intensity $\zeta_1 = 6 \times 10^{-12} \text{ s}^{-1}$, the scattered X-rays' intensity $\zeta_2 = 10^{-15} \text{ s}^{-1}$ and the corresponding penetration columns $N_1 = 1.5 \times 10^{21} \text{ cm}^{-2}$ or 0.006 g cm^{-2} and $N_2 = 7 \times 10^{23} \text{ cm}^{-2}$ or 3 g cm^{-2} are measured by integrating the gas density vertically. This expression for the X-ray ionization rate was fit by Bai & Goodman (2009) to Monte Carlo radiative transfer results from Igea & Glassgold (1999). We take the young star's X-ray luminosity to be $2 \cdot 10^{30} \text{ erg s}^{-1}$ based on Chandra observations in the Orion nebula (Wolk et al. 2005).

Finally, we take a radionuclide ionization rate

$$\zeta_{RN} = 7 \times 10^{-19} (f_{dg}/10^{-2}) \text{ s}^{-1}, \quad (9)$$

with the constant derived from Solar system measurements of the daughter products of the short-lived nuclide ^{26}Al (Umebayashi & Nakano 2009). Since the ^{26}Al is refractory and concentrated in the solids, and since the only solids well-mixed in the gas are the fluffy dust aggregates, the ionization rate is proportional to the aggregates' mass fraction f_{dg} .

Eqs. 6-9 define the ionization rate throughout the cold parts of the disk. To find the ionization state we need a model for the recombination chemistry. A complex network of chemical reactions is involved both in the gas phase and on the surfaces of dust grains (Semenov et al. 2004). However in the presence of grains, the results can be well-approximated with a simplified network (Ilgner & Nelson 2006). We apply the simplified model put forward by Okuzumi (2009). His key ansatz is that the grains have an approximately Gaussian charge state distribution. This holds if the grains are fluffy aggregates and (1) capable of holding large numbers of elementary charges, and (2) only weakly electrically polarized by approaching electrons and ions. The grain charge state distribution is then a function of a single dimensionless parameter Γ , the electrostatic energy between a charged grain and an incident electron, relative to the thermal energy.

Writing the equilibrium rate equations for the electrons and ions, with the latter averaged over all ion species, and using electron-grain and ion-grain collision cross-sections averaged over the Gaussian grain charge state distribution, one can solve simultaneously for the ion and electron densities in terms of the same parameter Γ . Requiring charge neutrality then yields a single equation whose root is Γ . We solve this equation, Okuzumi's eq. 30, to obtain the number densities of the ions and electrons and the mean and width of the grain charge distribution. Our fractal aggregates have dust-to-gas mass ratio f_{dg} and are made up of individual grains or monomers whose radius we choose between 0.005 and 5 μm .

The most abundant molecular ion is often HCO^+ , since energetic particles convert H_2 to H_2^+ which quickly reacts with CO. However at temperatures high enough for metal atoms to desorb from the grains and enter the gas phase, such molecular ions readily transfer their charge to the metals. The metal ions recombine more slowly and hence end up more abundant. As a representative metal we consider magnesium following Ilgner & Nelson (2006).

The gas quickly reaches a charge equilibrium in the presence of the fluffy aggregates, with electron and ion densities

$$n_e = \frac{\zeta(m_d/m_n) (\sqrt{1+2g} - 1)}{f_{dg} s_e u_e \sigma} \frac{1}{g \exp(-\Gamma)} \quad (10)$$

and

$$n_i = \frac{\zeta(m_d/m_n) (\sqrt{1+2g} - 1)}{f_{dg} s_i u_i \sigma} \frac{1}{g(1+\Gamma)}, \quad (11)$$

where

$$g = \frac{2c_t \zeta n_{\text{gas}}}{s_i u_i s_e u_e (\sigma \rho_{\text{gas}} f_{dg} / m_d)^2} \frac{\exp(\Gamma)}{1+\Gamma}. \quad (12)$$

Also c_t is the mean gas-phase recombination rate, and the dimensionless parameter $\Gamma = -\langle Z \rangle e^2 / (ak_B T)$ depends on the mean grain charge $\langle Z \rangle$ in units of the electron charge e , the grain radius a and ge-

ometric cross-section σ , and the temperature T . Other quantities are the electron and ion thermal speeds u_e, u_i and sticking probabilities on grains s_e, s_i for which we use Okuzumi’s expressions.

The grain charge state distribution is the Gaussian

$$n_{\text{dust}}(Z) = \frac{n_{\text{dust}}}{\sqrt{2\pi\langle\Delta Z^2\rangle}} \exp\left[-\frac{(Z - \langle Z \rangle)^2}{2\langle\Delta Z^2\rangle}\right] \quad (13)$$

with spread

$$\langle\Delta Z^2\rangle = \frac{1 + \Gamma}{2 + \Gamma} \frac{ak_B T}{e^2} \quad (14)$$

(Okuzumi 2009), where the total dust number density $n_{\text{dust}} = \rho f_{dg}/m_{\text{dust}}$. Approximating the grain charge state distribution by the Gaussian yields an overall charge-neutral plasma to high accuracy when the fluffy aggregates are made of at least a few hundred monomers each. In Appendix B we show the net charge that creeps in when the grains’ charge spread is too small to be represented with a Gaussian.

We compute the conductivity including the contributions from grains across the charge state distribution, along with the contributions from the electrons and ions. The free parameters are the individual grains’ size and mass, the dust-to-gas ratio, the ionization rate and the gas-phase recombination rate. Our choices for the parameters governing the ionization state are listed in Table 1. The gas-phase recombination is further discussed in the next section.

2.4. Gas-Phase Recombination Rate

A key weakness of this ionization recipe when applied over a large range of disk locations is that it does not capture the transition from one dominant ion to the next, and in particular between molecular ions and metals which occurs at the metals’ thermal desorption temperature. The recipe yields a total ion abundance using a recombination rate averaged over all ion species x :

$$n_i = \sum_x n_x, \quad c_t = \frac{\sum_x c_x n_x}{\sum_x n_x}. \quad (15)$$

Here we focus on the transition between our representative metal ion Mg^+ , with number density n_1 , and molecular ion HCO^+ , with number density n_2 . Under charge equilibrium, the metal ion number density is given by

$$\frac{\partial n_1}{\partial t} = n_2 n_3 \alpha - c_1 n_1 n_e - s_i u_i \sigma n_{\text{dust}} n_1 = 0, \quad (16)$$

where n_3 is the number density of metal atoms remaining neutral and $n[\text{Mg}] = n_1 + n_3$ the total number density of metal atoms in the gas phase. Also $c_1 = 3 \cdot 10^{-11}/\sqrt{T} \text{ cm}^3 \text{ s}^{-1}$ is the metal ions’ radiative recombination rate, $c_2 = 3 \cdot 10^{-6}/\sqrt{T} \text{ cm}^3 \text{ s}^{-1}$ the molecular ions’ dissociative recombination rate and $c_3 = 3 \cdot 10^{-9} \text{ cm}^3 \text{ s}^{-1}$ the molecular-to-metal ion charge transfer rate coefficient

(Ilgner & Nelson 2006). Our task is to determine the effective recombination rate coefficient (eq. 9 in Okuzumi (2009)) by finding the ratio of metal and molecular ion densities $y = n_1/n_2$ in

$$c_t = \frac{1}{1+y} (c_2 + yc_1). \quad (17)$$

First we determine the number density of thermally-desorbed metal atoms in the gas phase $n[\text{Mg}]$, which depends on temperature. As described in Appendix A we balance adsorption of Mg on grains with thermal desorption. The metal-to-molecular ion ratio and gas ionization state are obtained by applying Okuzumi’s recipe first assuming all the gas-phase metal atoms are ionized, and then iteratively correcting c_t to get the final y .

In the fiducial model disk, the ion Mg^+ proves to be the main source of free electrons at the midplane inside 5 AU. We introduce the concept of the *metal line*, the location at which a metal such as magnesium freezes out. In our fiducial model, the metal line lies entirely inside 8 AU where $T \simeq 100$ K (Fig. 2, top).

In Fig. 2 (bottom) we show contours of the dimensionless factor $g(\Gamma)$ introduced in eq. 12. For $g(\Gamma) \gg 1$ gas-phase recombination dominates. The isolines of $g(\Gamma)$ follow the gas density isolines in the outer disk ($r > 50$ AU), but in the inner disk this is no longer the case. Still it is safe to say that for gas densities $\rho < 3 \times 10^{-15}$ gcm^{-3} the recombination occurs mostly in the gas phase rather than on the grains. In the outer disk, or in the inner disk above 5 pressure scale heights, the gas ionization degree is therefore insensitive to the dust properties.

3. Magneto-Rotational Turbulence

The gas couples to the magnetic fields, and gas movements can bend the field lines, if the fields diffuse slower than they are advected. For protostellar disks, various bending length scales and advection time scales have been suggested. If we take the length scale to be the gas scale height H , and the time scale to be the differential rotation or shear time Ω^{-1} , then the induction and diffusion terms in the field evolution equation, $\nabla \times (\mathbf{v} \times \mathbf{B})$ and $\nabla \times (\eta \nabla \times \mathbf{B})$, are roughly ΩB and $\eta B/H^2$, leading to the condition $c_s^2/(\eta\Omega) > 1$ (eq. 35 in Wardle (2007)).

However the turbulence involves structures smaller than the gas scale height. The magnetic field is sub-equipartition with the gas, so the Alfvén speed v_A is less than the sound speed c_s and the MRI wavelength v_{Az}/Ω is less than the gas scale height c_s/Ω . Furthermore the poloidal field components B_Θ and B_r are weaker than the azimuthal component in 3-D MRI turbulence calculations (Miller & Stone 2000), allowing the poloidal components to be bent into sharper curves. This is borne out by the observation that the turbulent correlation lengths are anisotropic, with eddies reaching size H only in the azimuthal direction (Guan & Gammie 2011; Flock et al. 2012).

MRI turbulence under stratified conditions is probably sustained by the cycle in which (a) B_ϕ is buoyant and its rise generates B_Θ , (b) from B_Θ the MRI produces B_r , and (c) the shear makes

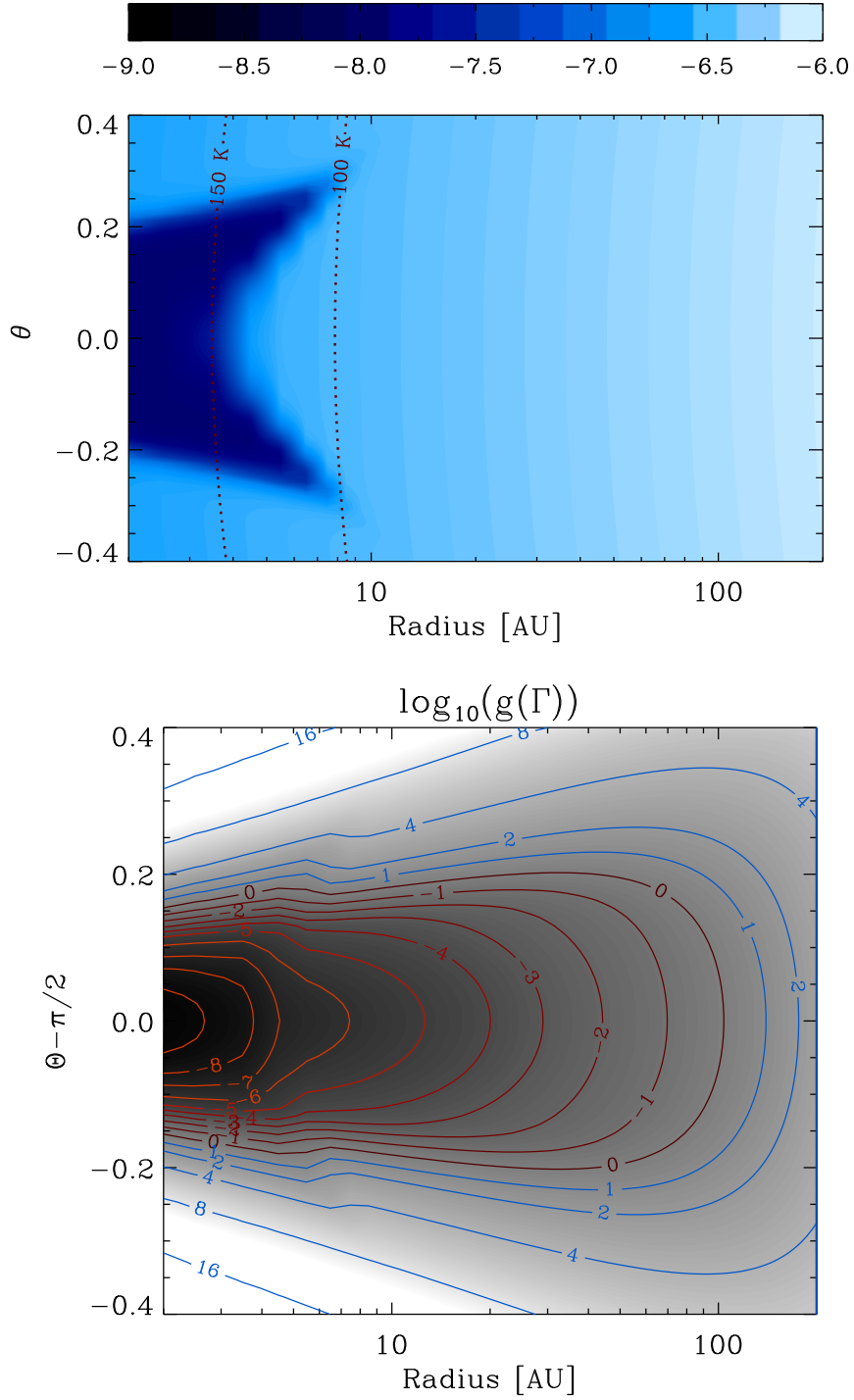


Fig. 2.— Left panel: logarithm of the total gas-phase recombination rate coefficient c_t in the fiducial model after eq. 17, in the $(r, \Theta - \pi/2)$ plane. Dotted lines mark where the temperature is 150 K (left) and 100 K (right). Right panel: logarithm of $g(\Gamma)$; gas-phase recombination dominates where $g(\Gamma) \gg 1$ (contour lines drawn in blue).

azimuthal field again from B_r (Tout & Pringle 1992; Hirose & Turner 2011). Step (b) in particular creates magnetic structures with a short vertical wavelength and may be the first step to shut down as the diffusivity is increased.

The appropriate criterion for sustained MRI turbulence is therefore that the fields diffuse across the MRI vertical wavelength in less than the MRI growth time. This corresponds to the dimensionless Elsasser number

$$\Lambda \equiv \frac{v_{Az}^2}{\eta\Omega} > 1, \quad (18)$$

where the Alfvén speed contains only the vertical component of the magnetic field. We use the Elsasser number criterion through the rest of this paper. Numerical calculations with an Ohmic diffusivity show that weak MRI turbulence operates down to

$$\frac{v_{Az}^2}{\eta\Omega} \simeq 0.1, \quad (19)$$

with larger, slower eddies and lower turbulent stresses (Sano & Miyama 1999; Sano et al. 2004; Simon et al. 2009). A similar condition holds for the ambipolar diffusivity (Bai 2011). We calculate the Elsasser number Λ in eqs. 18 and 19 including the Ohmic and ambipolar magnetic diffusivities, $\eta = \eta_O + \eta_A$. We neglect the Hall diffusivity in the MRI turbulence criterion because numerical results show it has weak effects when not more than two orders of magnitude greater than the Ohmic diffusivity (Sano & Stone 2002b).

In Fig. 3 we present schematically the dead zone and MRI-active region, separated by a transitional zone where $0.1 \leq \Lambda \leq 1$. In classical layered disk models (e.g. Armitage et al. (2001)) the disk consists of active and dead zones only. Here we further divide the dead zone into the transitional and more-thoroughly dead parts. The transitional part will prove important for trapping solids near the dead zone’s edge.

An important consequence of using the MRI wavelength rather than the density scale height is that the resulting Ohmic dead zone varies in size depending on the magnetic field strength. Ambipolar diffusion in contrast yields an Elsasser number independent of the magnetic field strength, since both the diffusivity and the squared Alfvén speed are proportional to the magnetic pressure.

We impose one more condition for MRI turbulence: since the instability grows quickly only on sub-thermal magnetic fields (Kim & Ostriker 2000), we require that the plasma beta $\beta = 8\pi P_{\text{gas}}/B^2 \geq 1$.

3.1. Magnetic Diffusivity

The electrons, ions and charged grains all contribute to the conductivity, while coupling to the magnetic field in varying degrees. A charged particle x has cyclotron frequency

$$\omega_x = |q_x|eB/(m_x c), \quad (20)$$

Table 1: Ionization parameters in the fiducial disk model

| Value | Units |
|--|----------------|
| $\zeta_{RN} = 7 \cdot 10^{-19} (f_{dg}/10^{-2})$ | s^{-1} |
| $\zeta_{CRO} = 5 \cdot 10^{-18}$ | s^{-1} |
| $\zeta_{1(XR)} = 6 \cdot 10^{-12}$ | s^{-1} |
| $\zeta_{2(XR)} = 1 \cdot 10^{-15}$ | s^{-1} |
| $N = 400$ | |
| $a = 20a_0$ | cm |
| $a_0 = 10^{-5}$ | cm |
| $f_{dg} = 10^{-4}$ | |
| $\sigma = \pi a^2$ | cm^2 |
| $\sigma_0 = \pi a_0^2$ | cm^2 |
| $s_i = 1$ | |
| $s_e = 0.3$ | |
| $d_0 = 1.4$ (ice) | $g\ cm^{-3}$ |
| $m_{dust} = \frac{4}{3} \pi a^2 a_0 d_0$ | g |
| $m_n = 2.3m_p$ | g |
| $m_{metal} = 24m_p, m_{HCO} = 29m_p$ | g |
| $c_3 = 3 \times 10^{-9}$ | $cm^3\ s^{-1}$ |
| $c_1 = 3 \times 10^{-11}$ (Mg) | $cm^3\ s^{-1}$ |
| $c_2 = 3 \times 10^{-6}$ (HCO) | $cm^3\ s^{-1}$ |

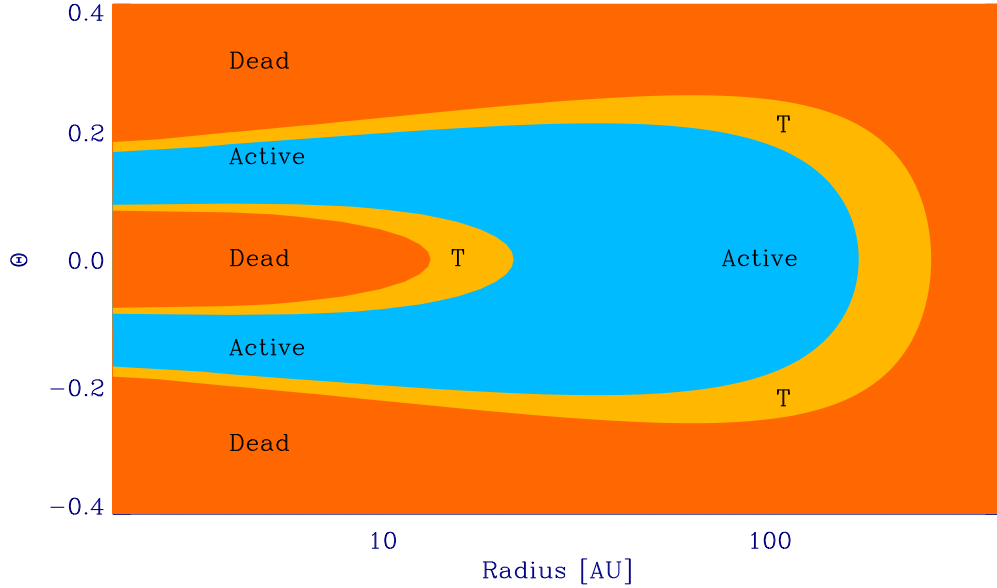


Fig. 3.— Schematic representation of the MRI-active region (blue), the transitional region labeled ‘T’ (yellow) and the magnetically dead zone (orange), based on evaluating the Elsasser number in eq. 27.

where $q_x e$ is the charge and m_x the mass. The damping time of the charged particle's motion relative to the neutrals is

$$\tau_x = \frac{m_n + m_x}{m_n} \frac{1}{n_n \langle \sigma v \rangle_{xn}}, \quad (21)$$

where $\langle \sigma v \rangle_{xn}$ is the momentum-transfer rate coefficient for colliding with neutrals, averaged over the Maxwellian velocity distribution. We adopt $\langle \sigma v \rangle_{en} = 10^{-15} \sqrt{128 k_B T / (9 \pi m_e)}$ for the electrons, and $\langle \sigma v \rangle_{in} = 1.9 \times 10^{-9}$ for the ions (Draine et al. 1983). The corresponding rate coefficient for the dust grains follows eq. 21 in Wardle & Ng (1999), where the collision speed is the neutrals' thermal speed since the grains' drift through the gas is subsonic. Putting together the cyclotron frequency and the collisional damping time, we obtain the parameter $b_x = \tau_x \omega_x$ that describes how well the charged particle couples to the magnetic field. For electrons, typically $b_e \gg 1$. The quality of coupling to the magnetic fields drops with the mass of the particle. The ions are more than 4 orders of magnitude heavier than the electrons, and the grains are orders of magnitude heavier still.

We treat the magnetic diffusivity as outlined by Wardle (2007), computing the electric currents from the number densities of charged particles obtained with Okuzumi's recipe. The current density in the partially-ionized gas is

$$\mathbf{J} = \sigma_O \mathbf{E}_{\parallel} + \sigma_H \hat{\mathbf{B}} \times \mathbf{E}_{\perp} + \sigma_P \mathbf{E}_{\perp} \quad (22)$$

where σ_O , σ_H , σ_P are the Ohmic, Hall and Pedersen conductivities (Cowling 1976; Wardle & Ng 1999),

$$\sigma_O = \frac{ec}{B} \sum_x n_x |q_x| b_x, \quad (23)$$

$$\sigma_H = -\frac{ec}{B} \sum_x \frac{n_x q_x b_x^2}{1 + b_x^2}, \quad (24)$$

$$\sigma_P = \frac{ec}{B} \sum_x \frac{n_x |q_x| b_x}{1 + b_x^2}. \quad (25)$$

The induction equation

$$\frac{\partial \mathbf{B}}{\partial t} = \nabla \times (\mathbf{u} \times \mathbf{B}) - \nabla \times \left(\eta_O \nabla \times \mathbf{B} + \eta_H (\nabla \times \mathbf{B}) \times \hat{\mathbf{B}} + \eta_A (\nabla \times \mathbf{B})_{\perp} \right) \quad (26)$$

then has diffusivities

$$\eta_O = \frac{c^2}{4\pi\sigma_O}, \quad \eta_H = \frac{c^2\sigma_H}{4\pi\sigma_{\perp}^2} \quad \text{and} \quad \eta_A = \frac{c^2\sigma_P}{4\pi\sigma_{\perp}^2} - \eta_O, \quad (27)$$

with $\sigma_{\perp} = \sqrt{(\sigma_H^2 + \sigma_P^2)}$.

3.2. Accretion Rate

Given the spatial distribution of the Elsasser number through the model disk, we estimate the mass accretion rate $\dot{M}(R)$ by summing the effective accretion rates within the magnetically-active, transitional and dead layers,

$$\dot{M} = 3\pi c_s H (\Sigma_{\text{ac}} \alpha_{\text{ac}} + \Sigma_{\text{T}} \alpha_{\text{T}} + \Sigma_{\text{dead}} \alpha_{\text{dead}}), \quad (28)$$

where subscripts * = “ac”, “T” and “dead” indicate the three respective layers, Σ_* are the layers’ mass columns and α_* are the corresponding stress parameters.

There is ample evidence that MRI turbulence yields an accretion stress $w_{R\phi}$ proportional to the magnetic pressure, that is, $\alpha_{\text{ac}} \equiv w_{R\phi}/P_{\text{gas}} \propto 1/\beta$, as long as $\beta > 1$ and the gas dominates the total pressure (Hawley et al. 1995; Bai & Stone 2011). In vertically-stratified disks, the stress parameter α increases with height as the local plasma beta decreases (Miller & Stone 2000), and the turbulent layers closest to the disk’s magnetically-dominated corona transport significant mass (Fleming & Stone 2003; Turner et al. 2010; Okuzumi & Hirose 2011). Once the plasma beta falls below unity, the stress drops off quickly (Miller & Stone 2000).

Since our magnetic pressure is independent of height, we make the stress uniform in the magnetically-active layer. We let the stress fall smoothly with decreasing plasma beta below a floor value β_f :

$$\alpha_{\text{ac}} = \begin{cases} \alpha_0 & \text{if } \beta \geq \beta_f \\ \exp\left(-\frac{2}{(\beta + \beta_f - 1)}\right) & \text{if } \beta < \beta_f. \end{cases} \quad (29)$$

For a fair match to shearing-box results we choose the floor value $\beta_f = 1.85$. The magnetically-active stress parameter α_0 is inversely proportional to the density, $\alpha_0 = \frac{\rho_{\text{mid}}(r)}{400\rho(r,\Theta)}$, where $\rho_{\text{mid}}(r)$ is the midplane gas density.

Our stress parameter in the transitional layer α_{T} behaves in the same manner with the disk height but is an order of magnitude weaker, having $\alpha_{\text{T}} = \alpha_{\text{ac}}/10$. In the dead zone, a non-zero Reynolds stress leads to $\alpha_{\text{dead}} = \alpha_{0,\text{mid}}/10^2$, where $\alpha_{0,\text{mid}}$ is the magnetically-active value of the stress parameter at the midplane (Dzyurkevich et al. 2010).

We investigate two approaches to the accretion stresses in disk regions with poor magnetic coupling. In the first we simply make the stress parameter a step function across the Elsasser number threshold (Martin et al. 2012; Martin & Livio 2012; Armitage et al. 2001). However, shearing-box MHD parameter surveys show a smooth roll-off in the stress at Elsasser numbers below unity (Sano et al. 2004), suggesting this simple approach might not capture all the accretion flow.

We therefore also consider a second approach in which the stress parameter varies smoothly with the Elsasser number. We use the upper bound on $\alpha(\Lambda)$ found in unstratified shearing-box ambipolar-MHD calculations by Bai & Stone (2011, their Fig. 4). Focusing on their results with net vertical magnetic flux corresponding to plasma beta 400, and adding a term for the non-zero

dead zone Reynolds stress, we obtain the approximate fitting formula

$$\alpha = \alpha_{\text{dead}} + \alpha_0 \frac{f(\Lambda)}{f(\Lambda = 10)}, \quad (30)$$

where

$$\log_{10} f(\Lambda) = -4 + \frac{k}{|k|} \sqrt{3k}, \quad (31)$$

and $k = \log_{10}(\Lambda + 1)$. This results in a smoothly-varying turbulent stress parameter. The two approaches yield identical accretion stresses for Elsasser number $\Lambda = 10$, but at other levels of magnetic coupling, the step-function under- or over-estimates the accretion rate: $\dot{M}^{\text{step}} > \dot{M}^{\text{smooth}}$ for $1 < \Lambda < 10$, and $\dot{M}^{\text{step}} < \dot{M}^{\text{smooth}}$ for $10 < \Lambda < 100$. Finally we require that the stress parameter not exceed 0.95, at which point transonic turbulent speeds would lead to rapid shock dissipation.

4. Results

In this section we present the dead zone calculated for the fiducial model disk and then vary the parameters in turn. The parameter study is summarized in Table 2.

The fiducial model’s dead zone is shown in Fig. 4 along with a version in which the monomers are enlarged to 1 μm , keeping the dust-to-gas ratio fixed. The Elsasser number divides the disk into dead and MRI-active regions. We further divide the dead zone into a thoroughly-dead part and the “transitional” zone, where the Elsasser number is less than one order of magnitude below the threshold for turbulence. Consider first the top left panel in Fig. 4. From the midplane to a few scale heights above, the Elsasser number changes by several orders of magnitude. By contrast the radial gradients are gradual, with the transitional region extending in the midplane from 8 to 20 AU. The conditions for MRI turbulence are satisfied at the midplane between 20 and 128 AU. The dead zone defined by Ohmic diffusion alone, using the Ohmic Elsasser number $\Lambda_O = v_{Az}^2/(\eta_O\Omega)$, has its customary almond shape (Sano et al. 2000), indicated in Fig. 4 by dotted lines where $\Lambda_O = 0.1, 1$ and 10. When the ambipolar diffusion is also taken into account, the dead zone is much larger and includes a transitional region whose outer edge is shaped like a fish’s tail. This shape is stronger still if the aggregates are made up of bigger monomers (Fig. 4, top right). The bottom plots in Fig. 4 show the importance of treating the transition from metal to molecular ion. Using Mg^+ throughout leads to dramatically overestimating the magnetic activity. On the other hand, HCO^+ alone accurately describes the dead zone’s outer edge but yields Elsasser numbers an order of magnitude too low in the MRI-active layers nearer the star. The transition between the two ions occurs at radii $3 \leq r \leq 8$ AU, where the temperatures are 150 K to 100 K (see also Fig. 2).

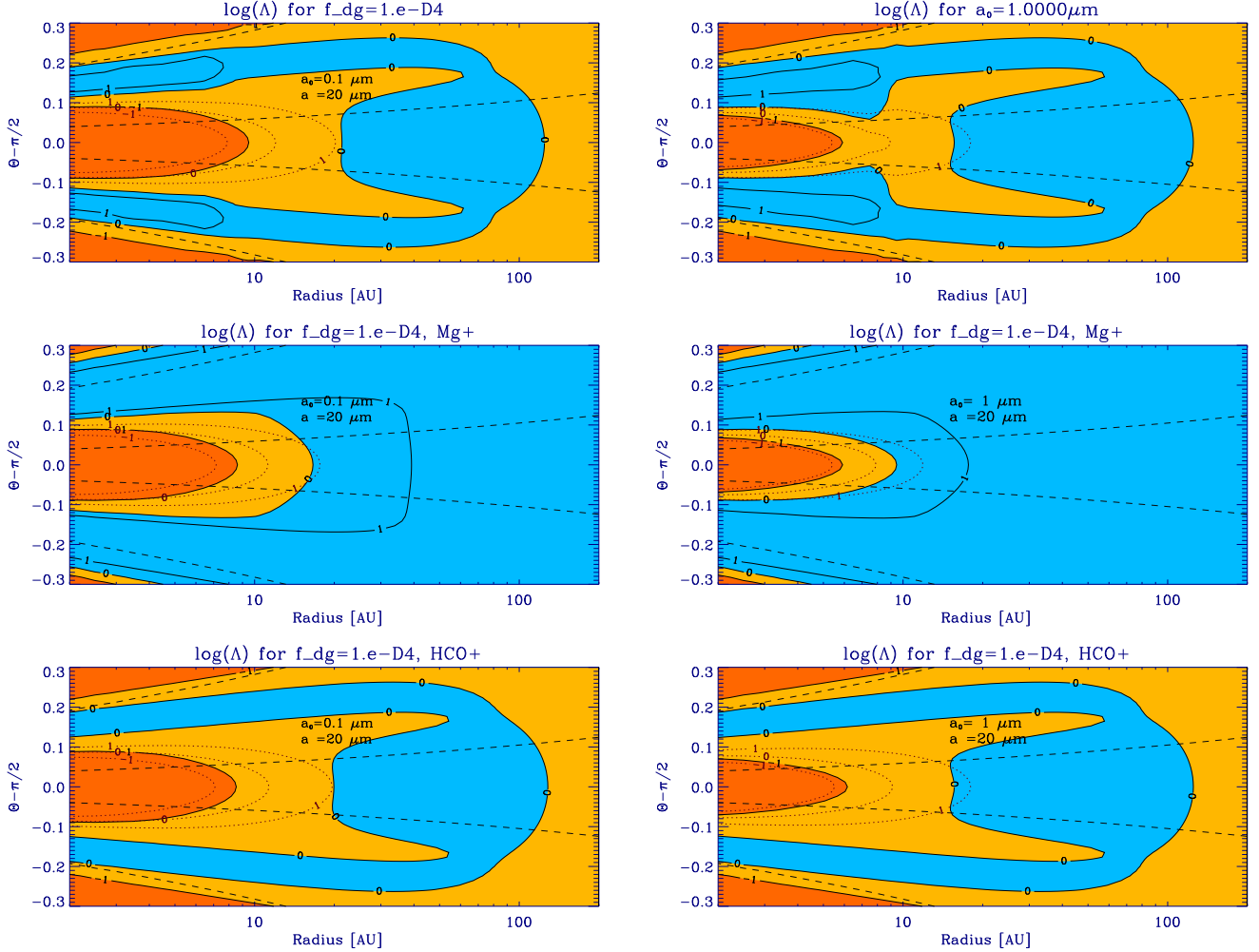


Fig. 4.— Dead, transitional and MRI-active zones for the fiducial model (left column) and a version with larger monomers $a_0 = 1 \mu\text{m}$ (right column). Blue regions are MRI-active, yellow are transitional and orange are MRI-dead. The top row includes the transition between the Mg^+ and HCO^+ ions, the middle row has Mg^+ everywhere and the bottom row has HCO^+ everywhere. Black solid contours indicate where the overall Elsasser number is 0.1, 1 and 10. Black dotted contours are the corresponding surfaces for the Elsasser number computed from Ohmic diffusivity alone. Black dashed lines mark heights H and $5H$.

4.1. Characterizing Ambipolar Diffusion

Figure 5 shows that ambipolar diffusion is more effective than Ohmic diffusion in damping MRI in our fiducial model and over a wide range of dust abundances. We therefore take a careful look at the criterion for MRI turbulence in the ambipolar diffusion regime.

Ambipolar diffusion has been characterized by two dimensionless numbers, the ion Reynolds number $Re_i = \gamma_i \rho_i / \Omega$ (Hawley & Stone 1998) and the ambipolar Elsasser number $\Lambda_A = v_{Az}^2 / (\eta_A \Omega)$ (Bai & Stone 2011). The Reynolds number accounts only for the ions, while the Elsasser number includes the contributions of all charged species. The question we ask here is, where is Re_i good enough, and where must the other plasma components be considered?

In Appendix C we show that the two numbers are equivalent if ions couple to the field and dominate the Pedersen conductivity, which is larger than the Hall conductivity. In Fig. 6 we therefore plot the ion coupling parameter b_i , the ions’ contribution as a fraction of the total Pedersen conductivity, the ratio of Hall to Pedersen conductivity, and the ratio of the electron number density to the ion number density, in the fiducial model disk. The ion Reynolds number is unreliable in two regions. The first is the dense interior, where collisions thoroughly decouple the ions from the fields. The second is the disk atmosphere above $6H$. There, gas densities are so low that grains can settle at supersonic speeds. This would make the grains the biggest contribution to the Pedersen conductivity. However since the gas drag and density profile are determined by heating and cooling, and potentially also by magnetic support, none of which we model in detail, we choose to neglect the settling for all our figures. Fuller treatment may be worthwhile in future.

Fig. 7 is a map of the ratio Re_i / Λ_A in the fiducial model disk. The two differ by a factor more than 1000 near 1 AU in the midplane. However the ratio is near unity in the large region shown in light gray, which includes the boundaries of the MRI-active region. The black dashed lines marking where $Re_i = 1$ almost overlap the yellow lines indicating where $\Lambda_A = 1$. Yet the curve where $Re_i / \Lambda_A = 1$ is in quite a different location. This is because even within the light-gray region the two numbers differ slightly (less than 1%).

The map of the MRI-active region looks basically identical whether drawn using the ion Reynolds or ambipolar Elsasser number. In our fiducial model, and in all models from Table 2, the ion Reynolds number is as good as the ambipolar Elsasser number for estimating the size of the MRI-active region. However, far from the active region’s edge, the ion Reynolds number can be unreliable as an estimator for the turbulent stress.

4.2. Magnetic diffusivities in the ion-dust limit

Ambipolar is the largest of the three diffusivities near the midplane at dust-to-gas mass ratio 10^{-2} (Fig. 5). This is unusual, as Ohmic diffusion typically dominates near the midplane for weak magnetic fields and Hall diffusion for stronger fields (Wardle 2007). We therefore examine

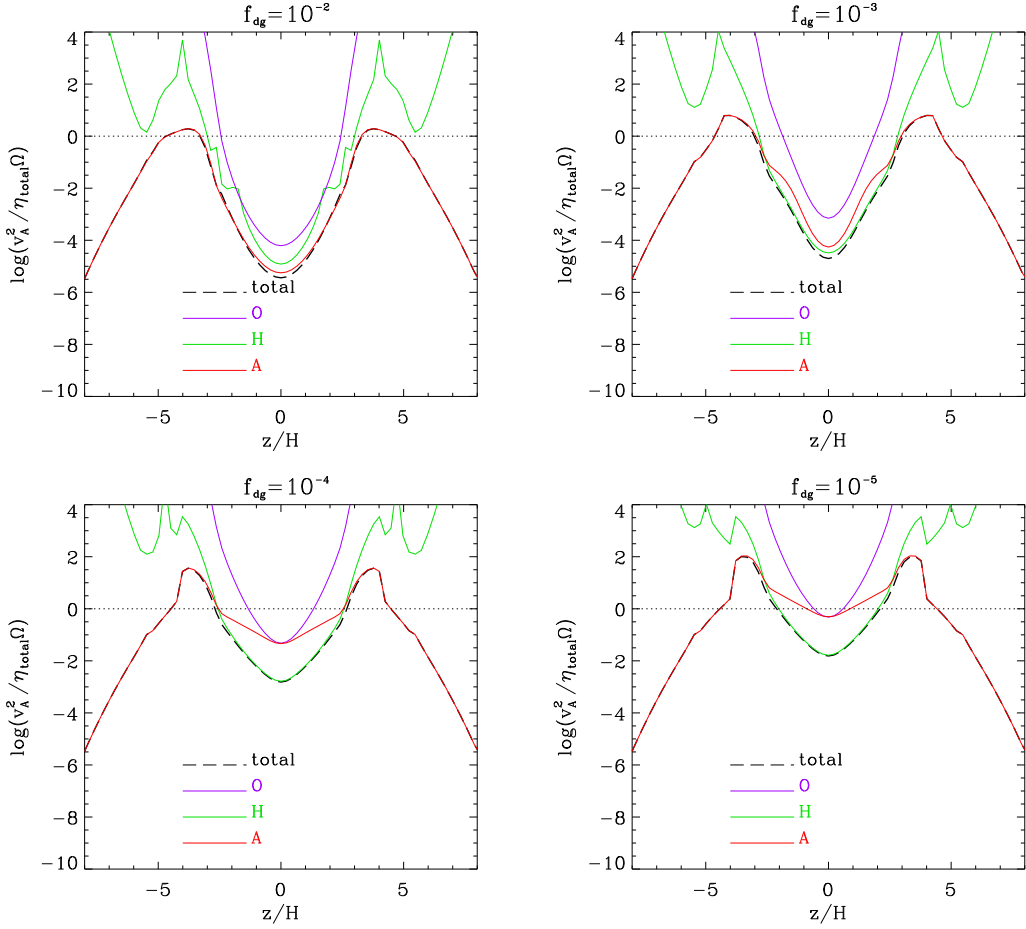


Fig. 5.— Contributions to the total Elsasser number (black dashed curves) from Ohmic diffusion (purple), Hall effect (green) and ambipolar diffusion (red) at radius 7.5 AU in the fiducial model disk and versions with dust-to-gas ratios from 10^{-2} (top left) to 10^{-5} (bottom right). The horizontal axis is the height in units of the pressure scale height, with $c_0 = c_s/u_{\text{Kepler}}$.

Table 2: Sets of models in the parameter study. The rows are the monomer radius a_0 , the dust-to-gas mass ratio in the fluffy aggregates f_{dg} , the disk mass in units of the stellar mass M_d/M_* , the surface density power-law index p , the temperature at 1 AU T_0 , the stellar mass in Solar masses M_*/M_\odot , the cosmic ray ionization rate outside the disk ζ_{CR0} (eq. 6), and the ionization rate due to radionuclides ζ_{RN} (eq. 9).

| Models | fiducial | Set 1 | Set 2 | Set 3 | Set 4 | Set 5 | Set 6 | Set 7 |
|----------------------------|--------------------|-------------------------|---|--|-------------------------|-------------------------|-------------------------|---|
| a_0 [μm] | 0.1 | [5 \rightarrow 0.001] | 0.1 | 0.1 | 0.1 | 0.1 | 0.1 | 0.1 |
| f_{dg} | 10^{-4} | 10^{-4} | [$10^{-2} \rightarrow 10^{-7}$] | 10^{-4} | 10^{-4} | 10^{-4} | 10^{-4} | 10^{-4} |
| M_d/M_* | 0.064 | 0.064 | 0.064 | [0.2 \rightarrow 1.5] \times $\times 0.064$ | 0.064 | 0.064 | 0.064 | 0.064 |
| p | 0.9 | 0.9 | 0.9 | 0.9 | [0.5 \rightarrow 1.5] | 0.9 | 0.9 | 0.9 |
| T_0 [K] | 280 | 280 | 280 | 280 | 280 | [150 \rightarrow 600] | [446 \rightarrow 650] | 280 |
| M_*/M_\odot | 1 | 1 | 1 | 1 | 1 | 1 | [0.4 \rightarrow 2] | 1 |
| ζ_{CR0} [s^{-1}] | $5 \cdot 10^{-18}$ | $5 \cdot 10^{-18}$ | $5 \cdot 10^{-18}$ | $5 \cdot 10^{-18}$ | $5 \cdot 10^{-18}$ | $5 \cdot 10^{-18}$ | $5 \cdot 10^{-18}$ | $5 \cdot [10^{-18} \rightarrow 10^{-15}]$ |
| ζ_{RN} [s^{-1}] | $7 \cdot 10^{-21}$ | $7 \cdot 10^{-21}$ | $7 \cdot [10^{-19} \rightarrow 10^{-24}]$ | $7 \cdot 10^{-21}$ | $7 \cdot 10^{-21}$ | $7 \cdot 10^{-21}$ | $7 \cdot 10^{-21}$ | $7 \cdot 10^{-21}$ |

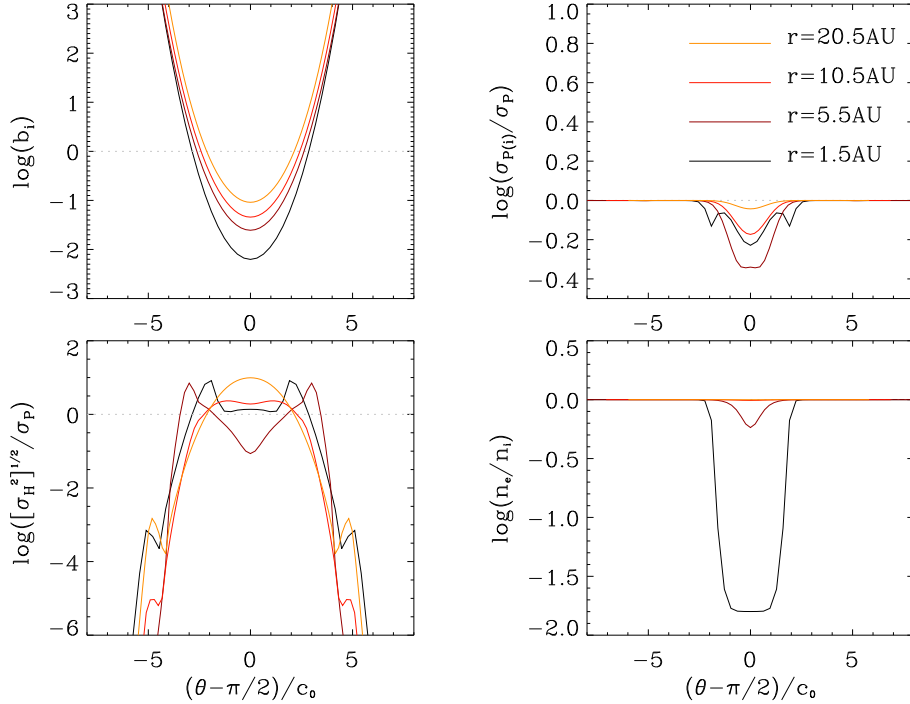


Fig. 6.— Top left: ion coupling parameter b_i versus height at four radii in the fiducial model disk. Top right: ratio of ion Pedersen conductivity to total Pedersen conductivity. Bottom left: ratio of absolute Hall conductivity to Pedersen conductivity. Bottom right: ratio of electron to ion number densities.

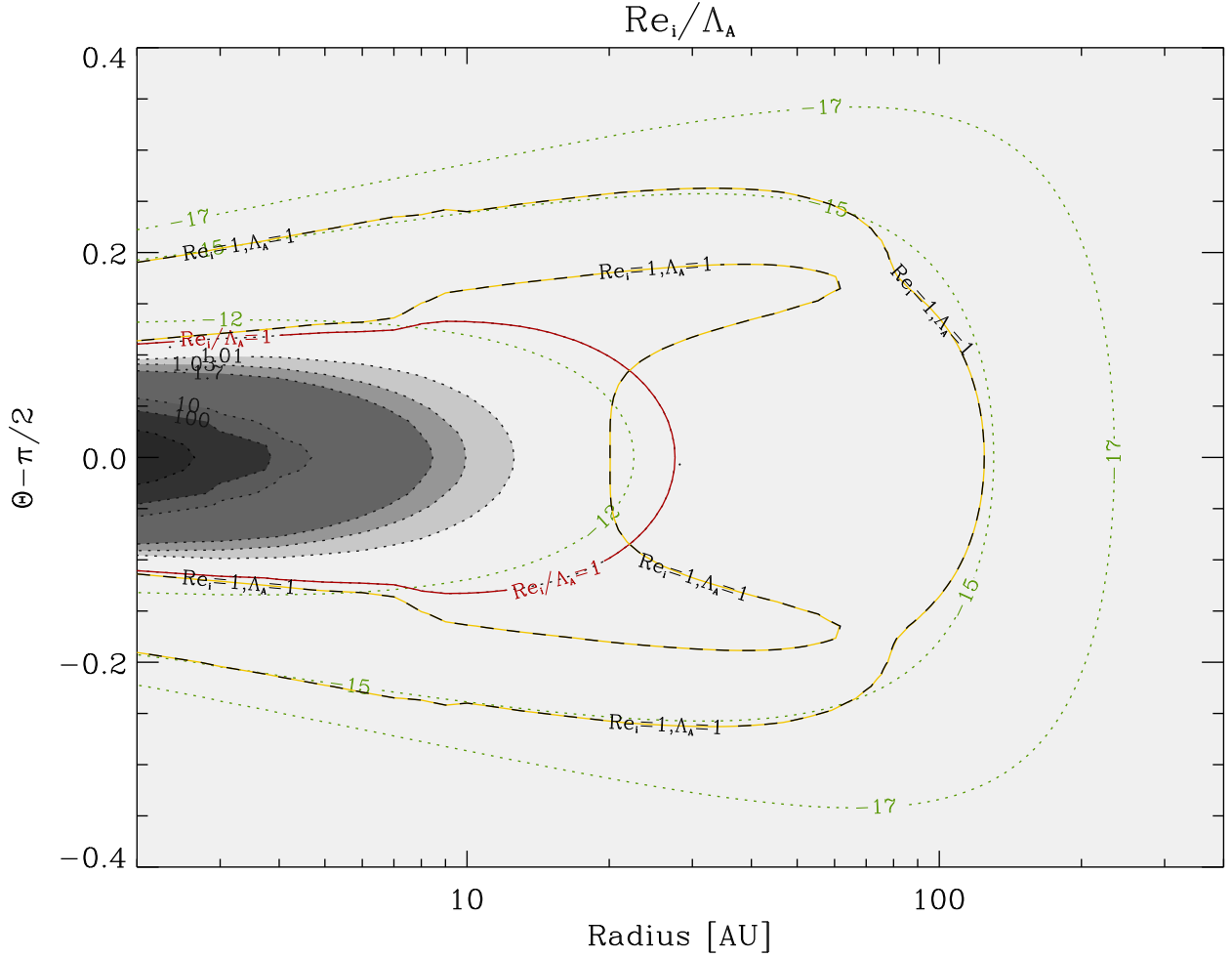


Fig. 7.— Gray contours and gray dotted lines show the ratio Re_i/Λ_A in the fiducial model disk. The red line marks $Re_i/\Lambda_A = 1$. On the black dashed line $Re_i = 1$ and on the nearly-overlapping yellow solid line $\Lambda_A = 1$, two estimates of the border of the MRI-active region. The green dotted lines are logarithmically-spaced isodensity contours labelled in g cm^{-3} .

the reasons. The ionization balance falls in the ion-dust limit, where the grains sweep up many electrons and ions, becoming the most abundant plasma component with a mean negative charge of a fraction of an electron. Even so, the grains’ large mass means they couple very poorly to the magnetic fields, leaving the Ohmic and Hall diffusivities dominated by the well-coupled electrons, and the Pedersen conductivity by the poorly-coupled ions:

- The Ohmic conductivity comes from the electrons because they couple best to the fields; $\sigma_O \propto nb$ in eq. 23, and $b_e \approx 1000b_i$, while in the ion-dust limit $n_e \approx n_i/100$ (Okuzumi 2009).
- The Hall conductivity also comes from the electrons since $\sigma_H \propto nb^2/(1+b^2)$ in eq. 24. The coupling $b_e \gg 1 \gg b_i$ means the electrons’ contribution $\approx n_e$ is greater than the ions’ $\approx n_i b_i^2$.
- The Pedersen conductivity is in the ions because they are more numerous than the electrons, while the two coupling parameters bracket the maximum at $b = 1$ in $\sigma_P \propto nb/(1+b^2)$ (eq. 25).

Consequently the Ohmic conductivity is greater than the Pedersen, which in turn is greater than the Hall, since $(\sigma_O \sim n_e b_e) > (\sigma_P \sim n_i b_i) > (\sigma_H \sim n_i/100)$. Thus in our eq. 27, $\sigma_\perp \approx \sigma_P$ and the ambipolar diffusivity $\eta_A \propto \sigma_P^{-1}$ is bigger than the Ohmic diffusivity $\eta_O \propto \sigma_O^{-1}$. The special circumstance leading to ambipolar dominance in the ion-dust limit is our chosen magnetic field strength, which couples the ions too little for them to contribute to the Hall conductivity, but enough to dominate the Pedersen conductivity.

For $f_{dg} < 10^{-3}$, the reduced grain surface area means the midplane near 7 AU no longer reaches the ion-dust limit. The ionization fraction is larger, the electron density is comparable to the ion density, and both exceed the density of the charged grains, which carry many electrons on average. The Ohmic and Hall conductivities are both larger in proportion to the increased electron density, while the Pedersen conductivity scales with the lesser increase in the ion density. As a result the Hall overtakes the Pedersen conductivity, giving the ordering $\sigma_O > \sigma_H > \sigma_P$. Since $\eta_H \sim 1/\sigma_H > \eta_A \sim \sigma_P/\sigma_H^2$, the largest diffusivity is the Hall one.

The Hall term is special in that it depends on the sign of the magnetic field, suppressing the MRI for one field direction and amplifying it for the other. It is unclear whether the Hall term has a strong impact on a turbulent eddy penetrating into the transitional or dead zone, as an eddy typically carries magnetic field of both signs. The importance of the Hall effect in the nonlinear evolution of the MRI remains to be clarified with further numerical calculations. Therefore we here confine ourselves to considering the Ohmic and ambipolar Elsasser numbers.

4.3. Magnetic Field Strength

One of the greatest uncertainties in modeling the magnetic coupling in protostellar disks is the strength and configuration of the magnetic field. A lower limit on the field strength is the mean Galactic field of $\sim 10 \mu\text{Gauss}$ (Beck & Hoernes 1996; Beck et al. 1996). An upper limit is

equipartition of the vertical magnetic field with the gas, which makes the shortest unstable MRI mode longer than the disk thickness. In our models the midplane plasma beta is independent of radius, while the magnetic pressure is independent of height (see eq. 5 in section 2.1).

The ambipolar Elsasser number is basically independent of the magnetic field strength, but the Ohmic Elsasser number is proportional to B^2 (eqs. 21, 25 and 27). Fig. 5 shows that the ambipolar Elsasser number is smaller than the Ohmic Elsasser number only by a small factor near the midplane. Thus in a magnetic field just a few times weaker, the MRI would be damped by Ohmic rather than ambipolar diffusion near the midplane. Another concern is above what height the disk is magnetically-dominated, with plasma beta less than unity. To clarify these points, we vary the midplane plasma beta from 10 to 10^6 . The corresponding magnetic fields are between 3.25 and 10^{-2} milligauss at 100 AU, where the field strength can potentially be measured using sub-millimeter polarization (Krejny et al. 2009). In Fig. 8 (left) we plot the radial locations where the Ohmic and ambipolar Elsasser numbers are 0.1 and 1, as functions of plasma beta. This range corresponds to the dead zone’s outer edge, which we call the transitional zone. Its width shows how gradual the transition is between dead and active zones. We see that the Ohmic dead zone grows with plasma beta. At $\beta > 4000$, Ohmic rather than ambipolar dissipation sets the outer dead zone boundary in the midplane. On the other hand, for strong magnetic fields such as 3 milligauss, or midplane plasma beta 10, the Ohmic dead zone lies deep within the ambipolar dead zone.

Choosing low midplane plasma beta also leaves the disk’s upper parts strongly magnetized and stable against MRI. In our fiducial model, the plasma beta is below unity above $3.5H$ (Fig. 8 right, green line). For a field strength at 100 AU matching the galactic field of $10 \mu\text{G}$ (plasma beta of 10^6), the magnetized region is only above $5H$ (Fig. 8, right). Note that ambipolar diffusion defines the dead zone’s *minimum radial extent*. A larger dead zone indicates that the fields are weak enough for the Ohmic diffusion to control the evolution of the MRI.

4.4. Monomer Size

Here we discuss the influence of monomer size on the shape of the MRI-active region (set 1, Table 2). The outer border of the active zone is well aligned with the gas isodensity surface $\rho = 10^{-15} \text{ g cm}^{-3}$. The active zone encloses an interior dead and transitional zone shaped like a fish tail. Outside 10 AU, the active zone is defined by ambipolar diffusion. The Ohmic diffusion plays hardly any role in the radial extent of the dead zone for the assumed magnetic field strength. However Ohmic diffusion is important for the dead zone’s vertical thickness in the inner disk. The transitional layer widens outside 8 AU, giving the fish-tail shape. The widening is caused by the switch from Mg^+ to HCO^+ as the main ion, leading to lower ionization fractions since the molecular ion recombines faster. For very small monomers, 0.005 (not shown) and $0.01 \mu\text{m}$ in radius, the active layers are thinner and separated from a midplane island of magnetic activity in the outer disk (Fig. 9, bottom). Also, the ratio Re_i/Λ_A deviates strongly from unity. Small grains couple better to the magnetic fields and participate in currents in the disk corona. Meanwhile in the

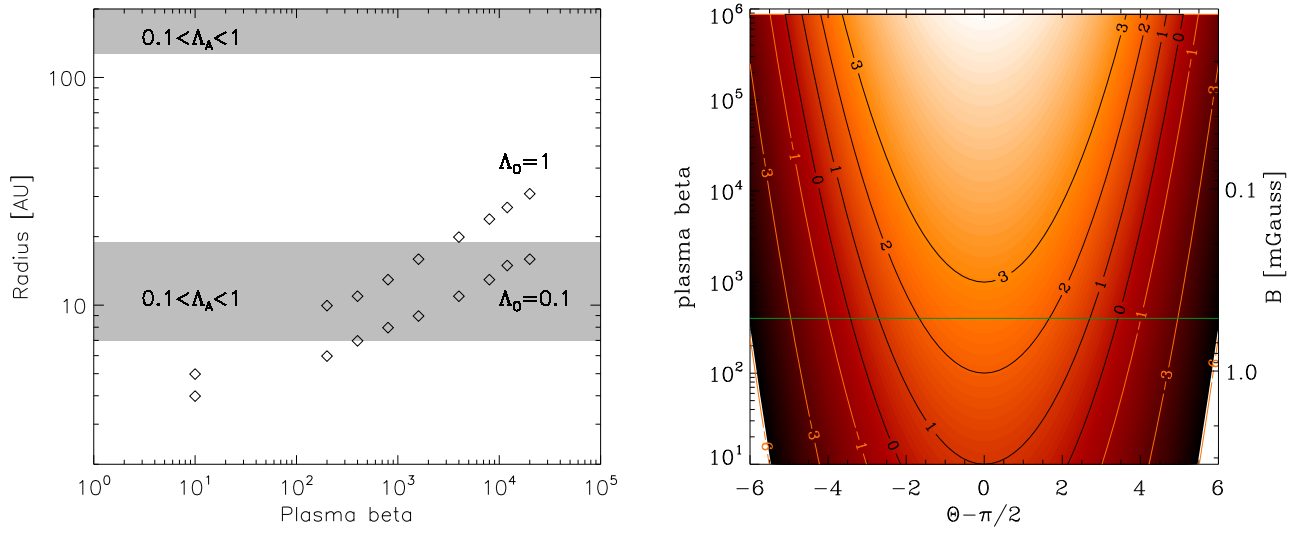


Fig. 8.— Left: The radial extents of the Ohmic and ambipolar transitional layers at the midplane in the fiducial disk model, as functions of the plasma beta parameter. Gray shading indicates where the ambipolar Elsasser number is between 0.1 and 1. Diamonds show Ohmic Elsasser numbers of 0.1 (bottom chain) and 1 (top chain). Right: Contours of plasma beta as a function of the height in pressure scale heights (horizontal axis) and the midplane plasma beta (vertical axis). On the right-hand vertical axis is the strength of the corresponding vertical magnetic field in Gauss at 100 AU. A green line marks our chosen midplane plasma beta parameter $\beta = 400$.

interior dead zone, the small grains readily sweep up free electrons, leaving $n_i \gg n_e$. These results suggest that the effects of very small grains such as PAHs are best characterized using the Elsasser number criterion, which includes the contributions of all the plasma components as outlined above in section 4.1.

The transitional zone gains in radial extent at the midplane as the monomer size decreases. For $a_0 = 1\mu\text{m}$, the transitional zone runs from 6 AU where $\Lambda = 0.1$ to 15 AU where $\Lambda = 1$, giving 9 AU of transition between $\alpha_{\text{dead}} \approx 10^{-5}$ and $\alpha_{\text{ac}} \approx 10^{-3}$ (section 3.2). For $a_0 = 0.01\mu\text{m}$, the transitional layer extends from 19 to 45 AU, a width of 26 AU.

The accretion rates are plotted against the distance from the star for the various monomer sizes in Fig. 10 using the approach set out in Section 3.2. Very small monomers with $a_0 \leq 0.01\mu\text{m}$ produce accretion rates below $10^{-8}M_{\odot}\text{yr}^{-1}$ at 1 AU. The biggest monomers, $a_0 = 5\mu\text{m}$, give a maximum in the accretion rate between 7 and 8 AU. At about 10 AU the accretion rate has a gap, related to the radial variation in the active layers' thickness shown in Fig. 9. When the stress parameter $\alpha(\Lambda)$ is given a step-function shape, the accretion rate jumps from $9 \times 10^{-8}M_{\odot}\text{yr}^{-1}$ at 7 AU down to 2×10^{-8} at 12 AU. Aggregates composed of the intermediate-sized monomers yield jumps almost as large: from 6.5 to $2 \times 10^{-8}M_{\odot}\text{yr}^{-1}$ for $a_0 = 1\mu\text{m}$, and from 5 to 2×10^{-8} for $a_0 = 0.5\mu\text{m}$.

However the accretion rate profile changes drastically when the smooth function is adopted for $\alpha(\Lambda)$. The accretion rate peaks near the metal line, and accretion is much slower in the outer disk. The reason is that the Elsasser number is very near unity along the whole midplane outside 10 AU, so that the smooth function yields a turbulent stress that varies slowly across the border between transitional and active zone.

4.5. Dust-to-Gas Ratio

In this section we vary the dust-to-gas ratio (set 2, Table 2), leaving other parameters unchanged from the fiducial model. The resulting dead zones and the ambipolar Reynolds-to-Elsasser number ratio are shown in Fig. 11. The radial extent of the transitional layer again shows striking variations. The transitional layer's midplane radial width is 25 AU, 12 AU, 7.5AU and 2 AU with dust-to-gas ratios 10^{-3} , 10^{-4} , 10^{-5} and 10^{-6} . From the shift in the dead zone shape with increasing dust depletion, we see that the fish-tail shape appears when the active surface layers merge with the midplane active zone (Fig. 11, top left and top right). At the lowest dust-to-gas ratio, the transitional layer splits into two pieces, located near 1.5 and 10 AU, and both about 2 AU in radial extent at the midplane (Fig. 11, bottom right). The MRI-active region's outer boundary again lies at the gas isodensity surface $\rho = 10^{-15}\text{g cm}^{-3}$.

The radial profiles of the accretion rate are shown in Fig. 12. For the step function $\alpha(\Lambda)$ and dust-to-gas ratios less than 10^{-5} , the accretion flow shows a gap from 10 to 12 AU. The deficit in the gap is as much as a factor of four for dust-to-gas ratio $f_{dg} = 10^{-6}$. However no such feature

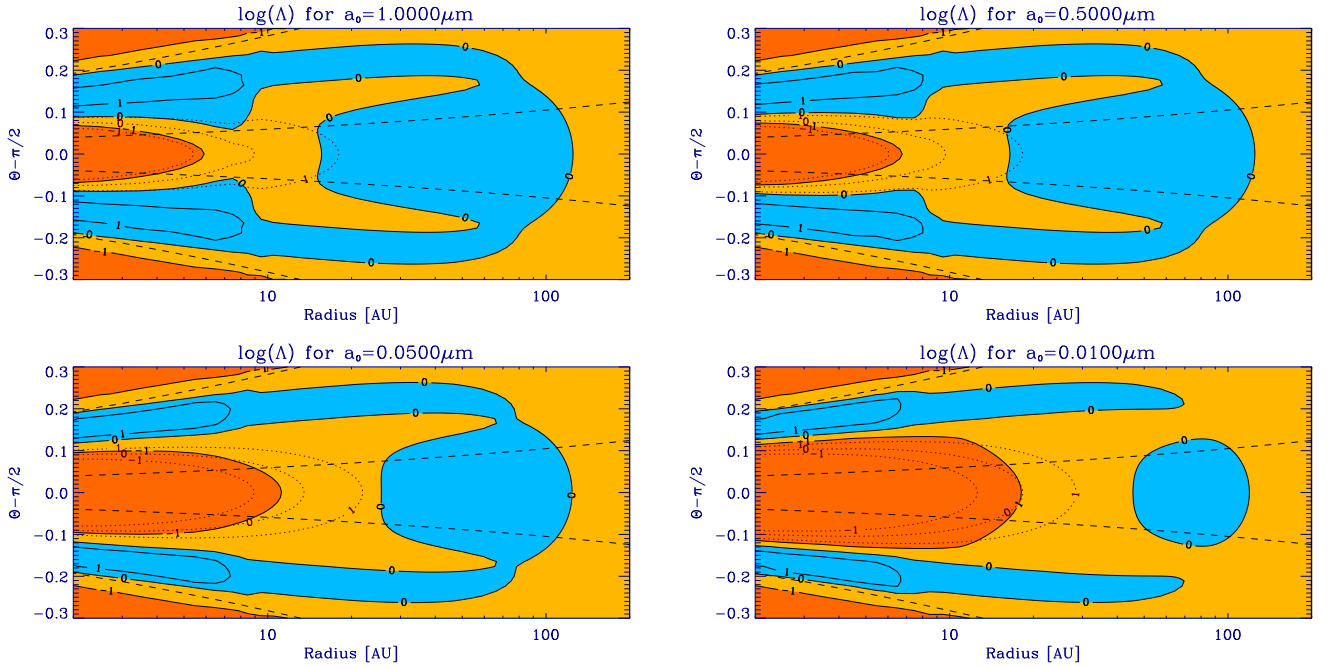


Fig. 9.— Contours of the total Elsasser number (black solid lines) and ohmic Elsasser number (black dotted lines) in disks containing fluffy aggregates composed of monomers of various radii. The MRI-active regions are shown in blue, the transitional regions in yellow and the dead zone in orange.

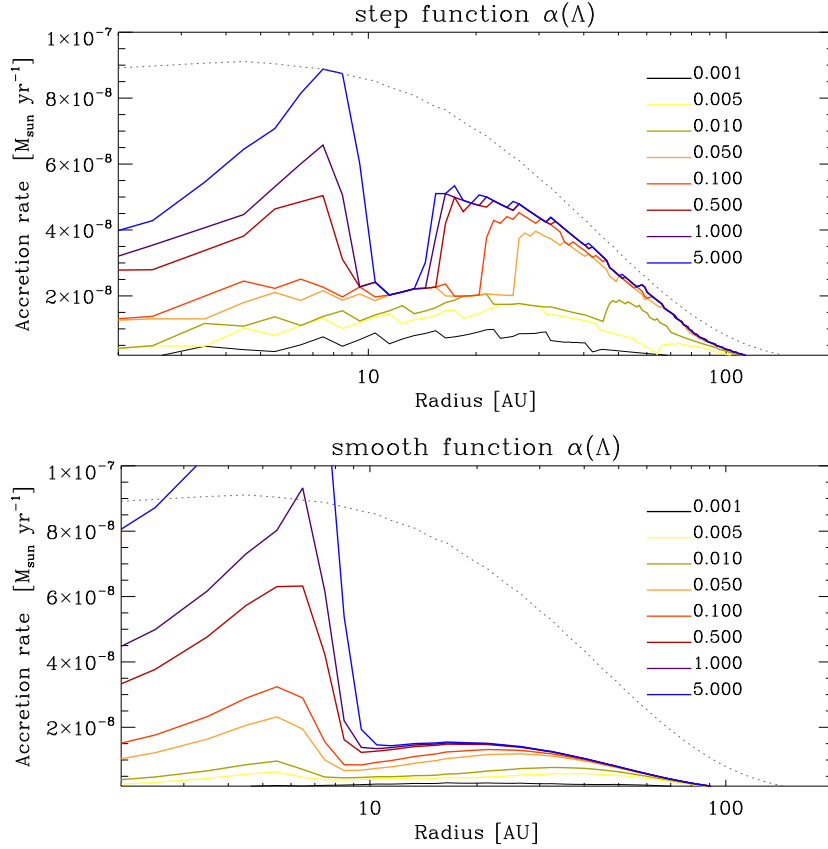


Fig. 10.— Accretion rate in solar masses per year for various monomer sizes. The dotted line shows the accretion rate for the case when the whole disk is active with the turbulent stress from eq. 29. Note that the smooth-function turbulent stress can lead to higher accretion rates in the $\Lambda > 10$ regions (see section 3.2).

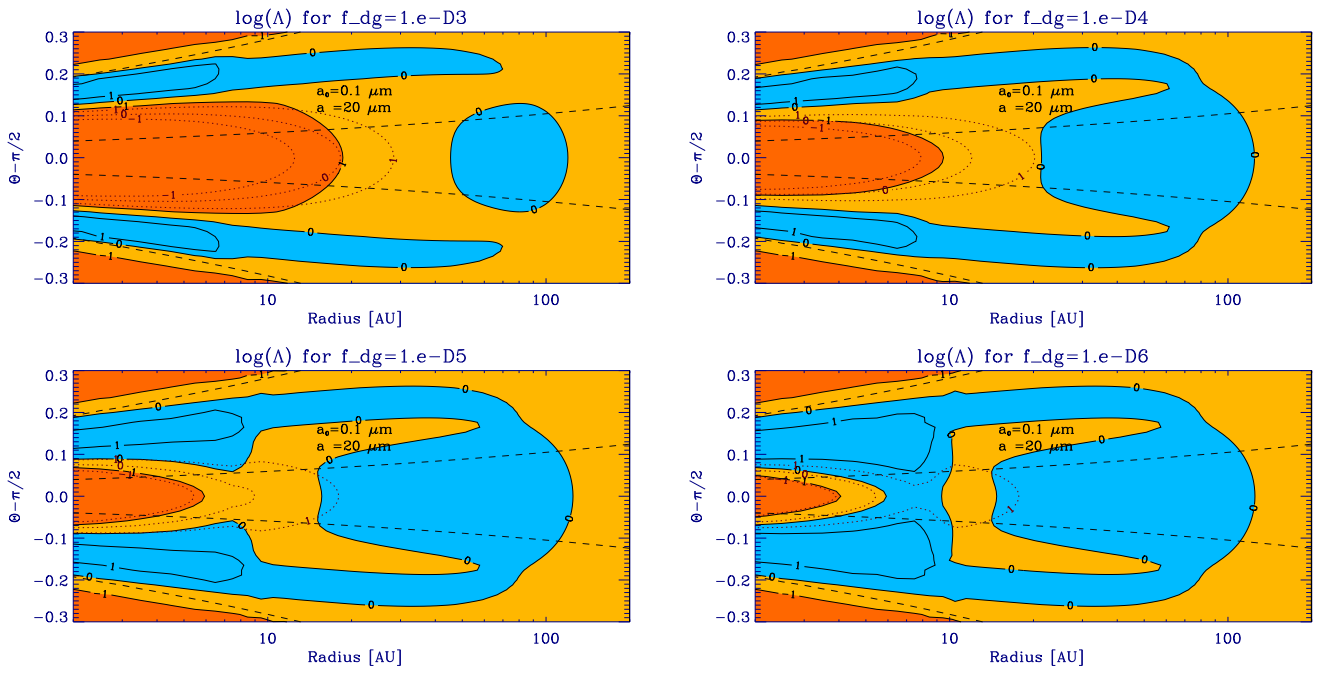


Fig. 11.— MRI-active regions appearance for various dust-to-gas ratio, see also Fig. 9. Colors and symbols are as in figure 9.

appears with the smooth $\alpha(\Lambda)$ function. Instead the accretion rate steps up inside the metal line, located between 7 and 10 AU, and the dead zone edge has no clear signature in the radial accretion rate profile.

4.6. Disk Mass

In set 3 from table 2, we vary the disk mass by scaling the fiducial model’s densities from eq. 3 (section 2.1). Increasing the mass makes more of the outer disk active, if we hold fixed the ratio of gas to magnetic pressure (Fig. 13). The reason is that higher densities make the ambipolar diffusion term less important relative to the induction term. The outermost border of the active zone shifts from 100 AU for the disk with $M_{\text{disk}} = 0.5M_{\text{fiducial}}$ to 140 AU for $M_{\text{disk}} = 1.5M_{\text{fiducial}}$, following the gas isodensity contour $\rho = 10^{-15} \text{ g cm}^{-3}$. At the same time, increasing the disk mass has little effect on the location and thickness of the active layers at higher latitudes. The active layer base simply moves slightly further from the midplane, as does the layer absorbing the ionizing cosmic rays and X-rays. The active layer becomes a little thinner because its top is still constrained by the requirement that magnetic pressure is not too much greater than gas pressure.

For the smallest disk mass in set 3 ($0.2M_{\text{fiducial}}$) MRI-active layers are found only at the higher latitudes, and the midplane is either dead or transitional. For larger disk masses, the midplane active island appears (Fig. 13, top right). In the two most massive disks from set 3, the active surface layers and midplane island merge. Over the same mass range, the interior dead zone grows due to the reduced ionization at the higher mass columns.

The transitional region between active and dead zones generally narrows with increasing disk mass, as the expanding inner dead zone approaches the expanding outer active island. The transition region is 13 AU, 12 AU and 10 AU wide for $M_{\text{disk}} = 0.5, 0.8$ and $1.5M_{\text{fiducial}}$. At the lowest disk mass, the transitional region stretches in the midplane from 4 to at least 200 AU. A substantial volume is thus capable of MRI turbulence at reduced levels.

The radial profiles of the accretion rate are shown in Fig. 14. Note that we keep the dust-to-gas ratio and monomer size same as in the fiducial model. The accretion rate is about $10^{-8} M_{\odot} \text{ yr}^{-1}$ at our inner boundary. For the smooth $\alpha(\Lambda)$ function the accretion rate dips at 9-10 AU near the metal line. In the more massive disks, the accretion profile becomes less dependent of mass.

The radial profiles of the accretion rate are shown in Fig. 14. Note that we keep the dust-to-gas ratio and monomer size the same as in the fiducial model. The accretion rate is about $10^{-8} M_{\odot} \text{ yr}^{-1}$ at our inner boundary. For the smooth $\alpha(\Lambda)$ function the accretion rate dips at 9-10 AU near the metal line. In the more massive disks, the accretion profile is almost independent of the mass.

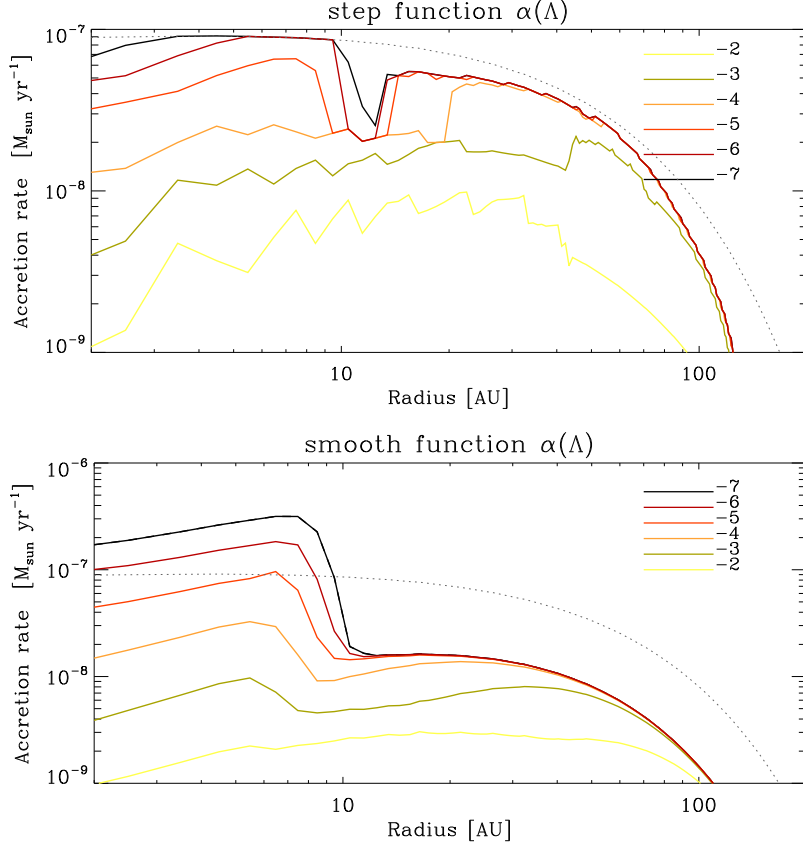


Fig. 12.— Accretion rate in solar mass units per year calculated for the MRI-active surface density and for $\beta > 1$ disk regions, for disks with various dust-to-gas ratios, $\log(f_{dg}) = [-2, -3, -4, -5, -6, -7]$. The dotted line shows the accretion rate for the case when whole disk is active with the turbulent stress taken from eq. 29. Note that the smooth-function turbulent stress can lead to higher accretion rates in the $\Lambda > 10$ regions (see section 3.2).

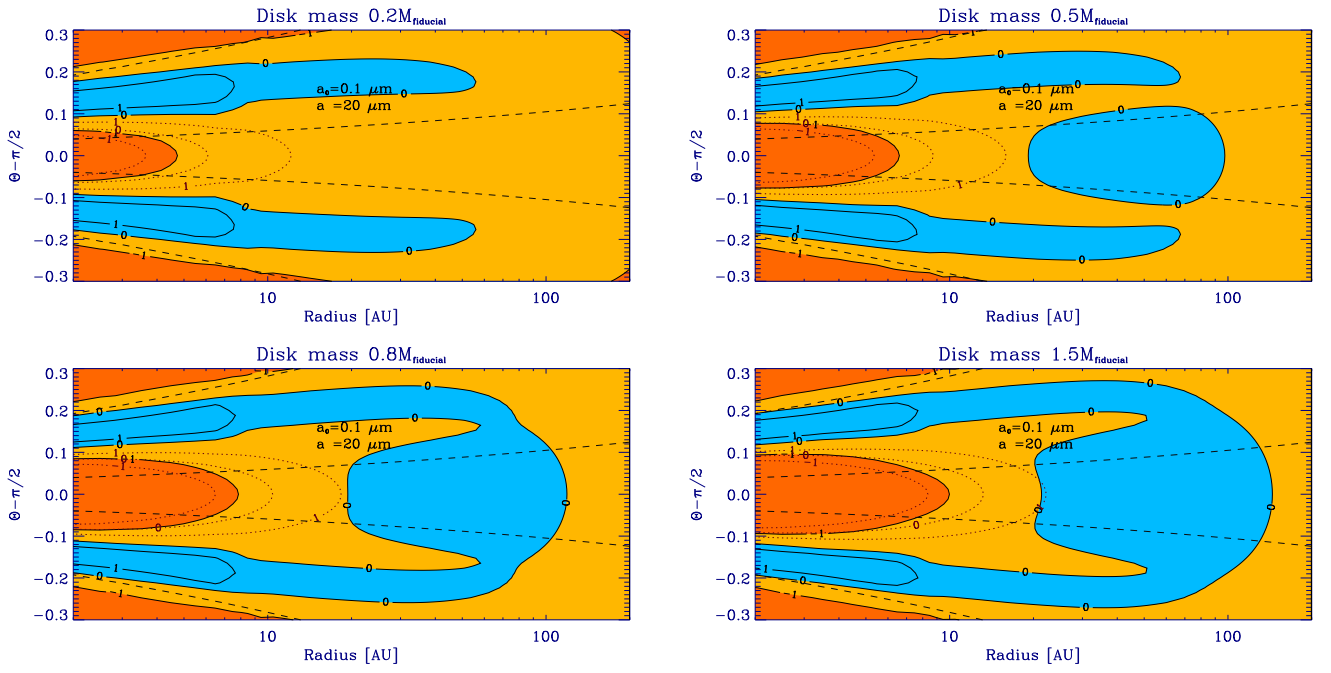


Fig. 13.— MRI-active regions’ appearance for disk mass 0.2, 0.5, 0.8 and 1.5 times the fiducial model. Colors and symbols are as in figure 4.

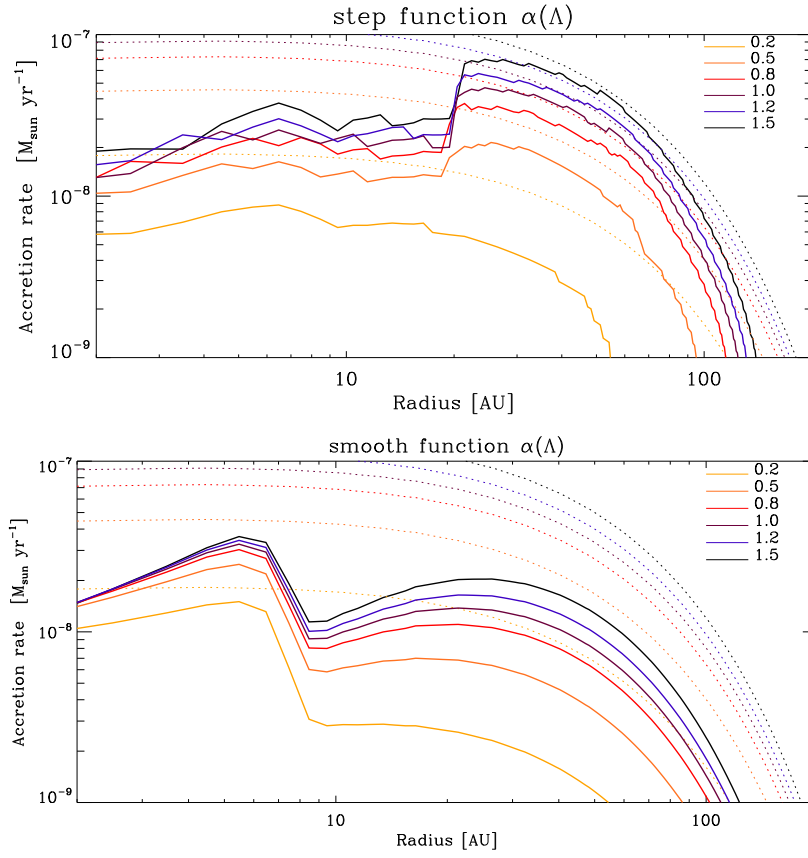


Fig. 14.— Accretion rate vs. radius in set 3 where the disks have masses 0.2, 0.5, 0.8, 1, 1.2 and 1.5 times the fiducial model. Dotted lines show the accretion rates if the disks were active throughout.

4.7. Surface Density Slope

In set 4 (Table 2) we vary the power-law index p in the surface density profile $\Sigma \propto r^{-p}$ from 0.5 to 1.5, keeping the disk mass and other parameters as in the fiducial model. The slope $p = 0.5$ is frequently adopted for numerical simulations (Fromang & Nelson 2006; Dzyurkevich et al. 2010; Flock et al. 2011). Millimeter interferometer measurements of the dust continuum emission yield a median index $p = 0.9$ (Andrews et al. 2009), while Hayashi’s minimum-mass Solar nebula model has $p = 1.5$ to approximate the distribution of mass in the Solar system.

With increasing surface density slope, the active zone expands outward from 100 AU to 195 AU (Fig. 15). At the same time the midplane dead zone thickens near 1 AU. For slopes p between 0.5 and 1.3 we obtain a single MRI-active region with a fish-tail shaped transitional layer. For $p = 1.5$ the outer disk’s low densities make the ambipolar diffusion stronger still. The transitional region is larger and isolates the magnetic activity in the two surface layers from the midplane island of activity. The transitional layer between the island and active layers at 50 AU (Fig. 15, bottom right), is only about one scale height thick. As MRI turbulence can overshoot the dead zone boundary by a scale height (Turner et al. 2010), the transitional layers could be turbulent thanks to the activity above and below.

In Fig. 16 we plot the accretion rates for the models in set 4. The inner border of the MRI-active region moves inward very little as the slope is increased. Similar to the results in the previous section, the accretion flow shows no gaps under the step-function $\alpha(\Lambda)$. The accretion rate is about $10^{-8} M_{\odot} \text{ yr}^{-1}$ at our 1 AU inner boundary. For the smooth $\alpha(\Lambda)$ function, \dot{M} peaks near the metal line. The accretion rate dip is deeper for shallower surface density profiles.

4.8. Temperature

Here we explore Set 5 (Table 2) in which we vary the gas temperatures. The domain we consider remains too cool for significant thermal ionization. Nevertheless the temperature is important for the conductivity because it regulates the disk thickness and hence the gas density, determines the gas-phase metal abundance, and sets the particles’ thermal speeds. We consider a range of temperatures from those observed at the starlight-heated surfaces of disks in nearby star-forming regions (Bouwman et al. 2001; Furlan et al. 2009) down to those inferred for the disk midplanes through radiative transfer modeling (Chiang & Goldreich 1997; Dullemond et al. 2007). We consider temperatures at 1 AU, T_0 , between 150 and 600 K, keeping the temperature’s radial power-law slope constant at -0.5 .

The resulting dead zones are shown in Fig. 17. In each case the MRI-active layers contract across the radius where the metal ions freeze out. The magnesium in our models freezes out at 2.5 AU if $T_0 = 180$ K, 4.5 AU if 280 K and 11 AU if 350 K. At $T_0 = 450$ K the MRI-active layers reach deep towards the midplane. We observe that the transitional layer’s fish-tail shape is present

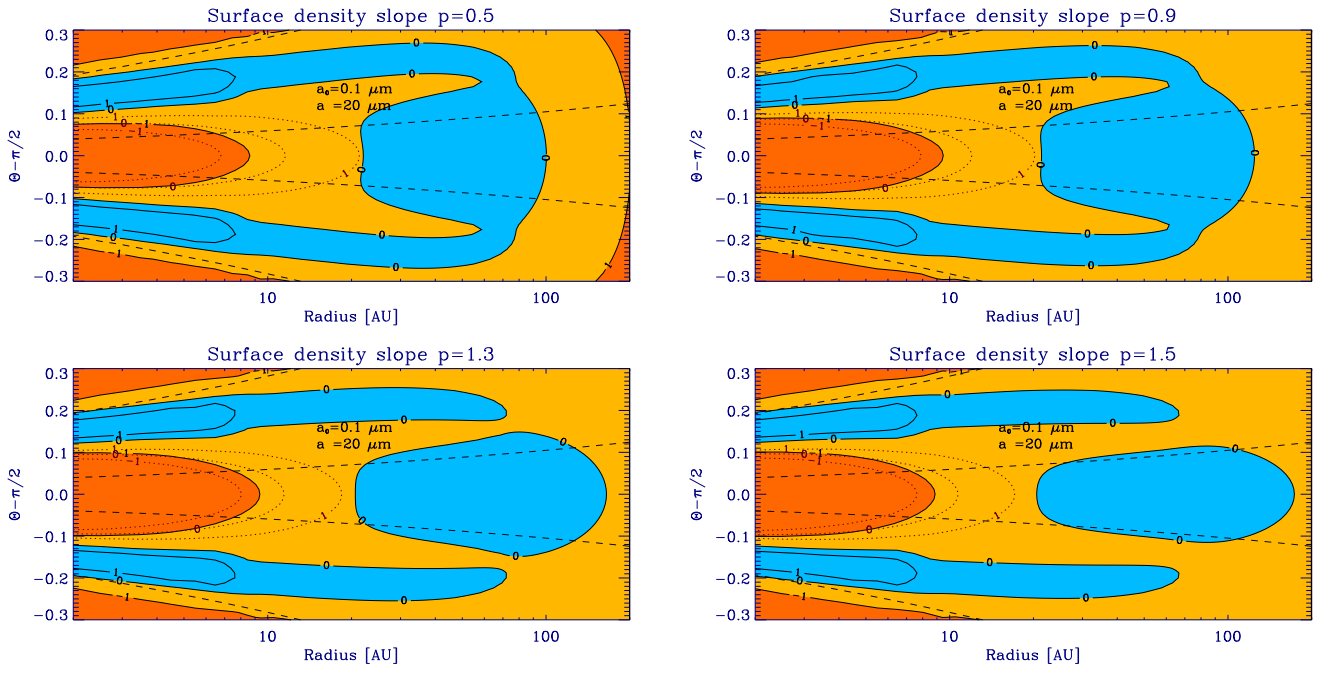


Fig. 15.— MRI-active regions appearance for surface density slope 0.5, 0.9, 1.3, 1.5, assuming a constant disk mass. Colors and symbols are as in figure 4.

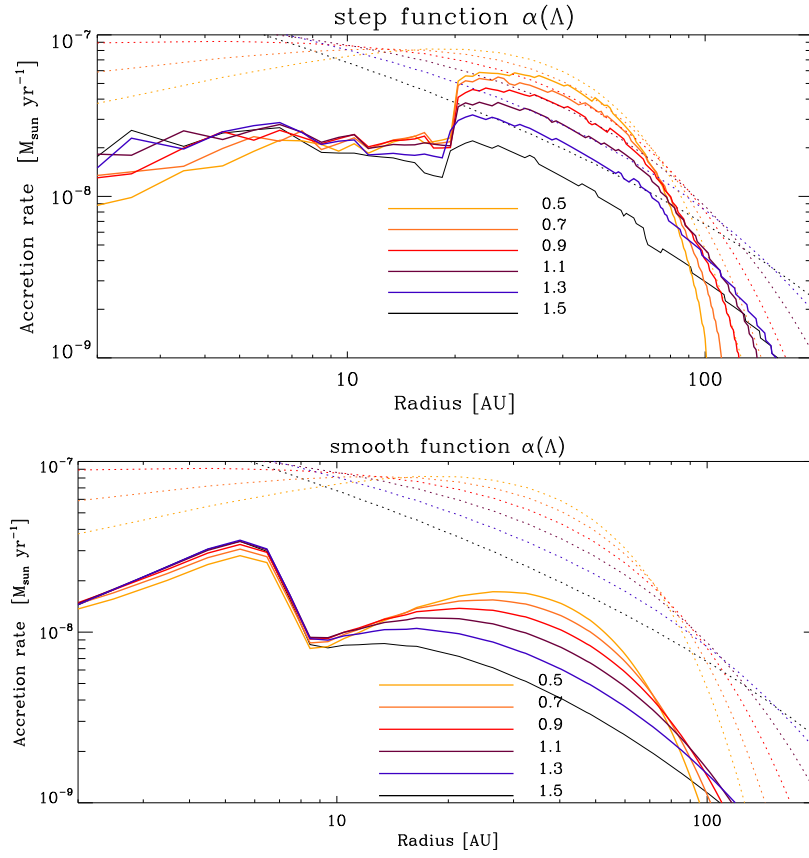


Fig. 16.— Accretion rate vs. radius in the disks with surface density slopes $p = 0.5, 0.9, 1.3$ and 1.5. Dotted lines show the accretion rates if the disks were active throughout.

only for $T_0 < 450$ K. For still higher temperatures, simple almond-shaped dead and surrounding transitional zones appear. The remnants of the fish-tail appear as islands in yellow roughly $2H$ above and below the midplane (Fig. 17, bottom). Although the islands stretch over several tens of AU in radius, their vertical thickness is less than one scale height, and they could conceivably be activated by the neighboring better-coupled regions.

The accretion rates for the models in set 5 are shown in Fig. 18. The islands of transitional coupling for temperatures T_0 from 450 to 600 K, seen in yellow in the bottom panels of Fig. 17, lead to small reductions in the accretion rate if we take $\alpha(\Lambda)$ to be a step function. If we instead use the smooth $\alpha(\Lambda)$ function, the accretion rate peak shifts outward following the isotherm $T \approx 100$ K, reaching 50 AU for the hottest disk (Fig. 18, bottom).

4.9. Stellar Mass

In set 6 (Table 2) we vary the stellar mass, which determines the orbital frequency, and through the vertical component of gravity affects the disk’s gas density. Furthermore the stellar luminosity grows with the stellar mass, affecting disk temperatures. We let the disk mass be proportional to the stellar mass, $M_{\text{disk}} = 0.064M_*$. Luminosities for stars between 0.3 and $2 M_\odot$ are taken from evolutionary tracks computed with the STELLAR code (Bodenheimer et al. 2007). For simplicity we neglect the influence of the gas accretion on the evolutionary tracks.

The stellar luminosity is plotted vs. the stellar mass in Fig. 19. We choose the time-step closest to 1 Myr as a typical age for disk-bearing stars. From the luminosity we reconstruct temperatures in the circumstellar disk as follows. The location of the dust sublimation front, where the temperature is about $T_s = 1500$ K, can be calculated as follows:

$$R_{in} = R_* \left(\frac{T_*}{T_s} \right)^2 = \left(\frac{L_*}{4\pi\sigma T_s^4} \right)^{1/2}. \quad (32)$$

From this point we assume the temperature falls off as $T = T_s \sqrt{(R_{in}/R)}$ corresponding to the optically-thin approximation used in the minimum-mass Solar nebula model on which our fiducial model is based. This overestimates the temperature since the disk is optically-thick, but our point here is to see whether the dead zone depends on the temperature.

For masses 0.4, 0.8, 1.2, 1.6 and $2 M_\odot$, the temperatures at 1 AU are 446.8, 518.7, 559.3, 604.6 and 650.9 K, respectively. The Solar-mass star aged 1 Myr has a higher luminosity than our fiducial model, yielding a temperature at 1 AU of 532.3 K instead of 280 K.

Higher luminosities stretch the metal-dominated region further from the star than in the fiducial model (Fig. 20). The Elsasser number $\Lambda = 10$ contour stretches along with the Mg^+ -dominated region, reaching 20 AU for the $0.4 M_\odot$ star and 45 AU for the $2 M_\odot$ star. When the metal-dominated region reaches much beyond 10 AU, the fish-tail shape no longer appears in the transitional layer. Disks around stars with masses 0.4 to $1 M_\odot$ (top panels in Fig. 20) have once

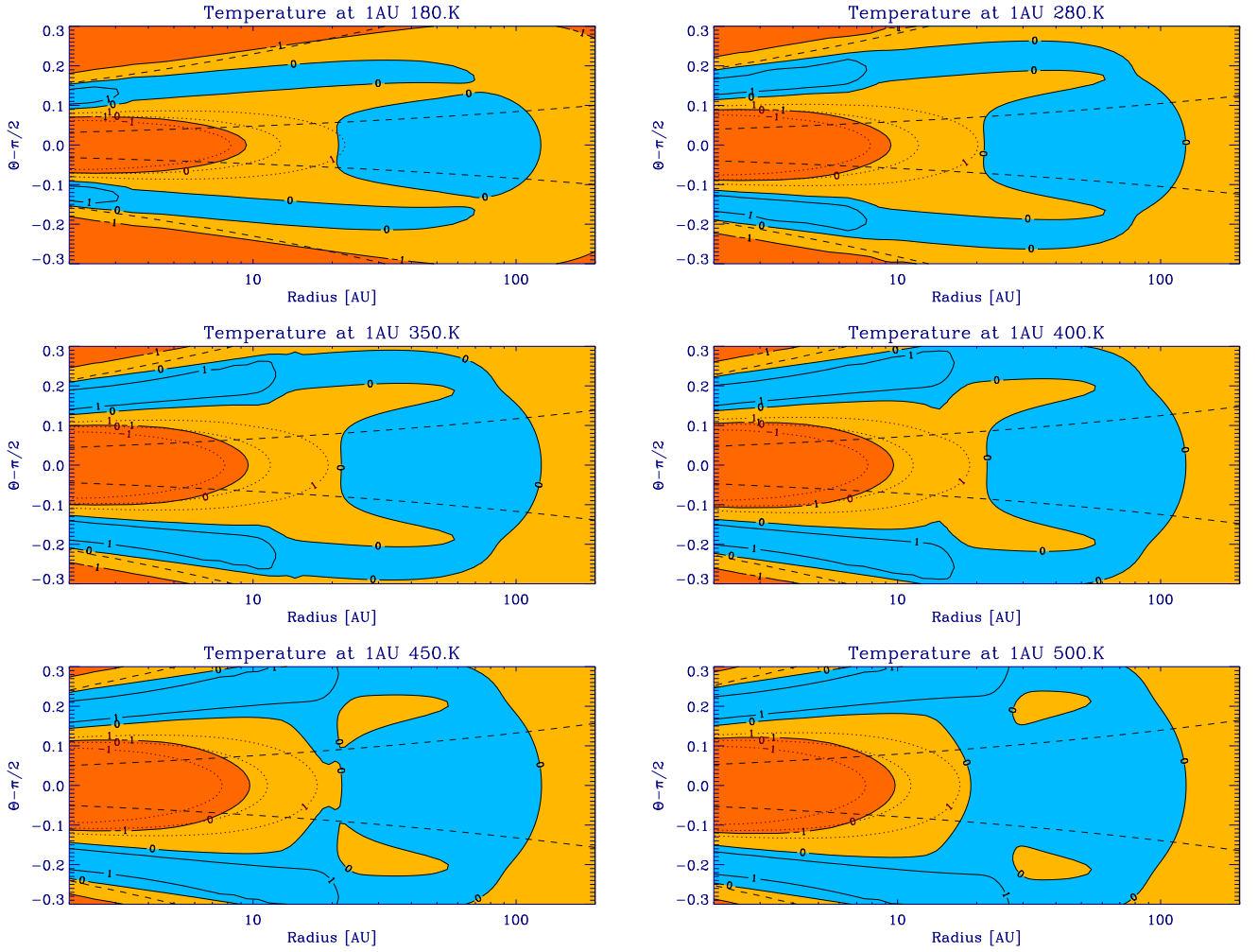


Fig. 17.— Magnetic coupling maps for disks with a range of temperature profiles $T = T_0(r/1AU)^{-0.5}$, with $T_0 = 180, \dots, 500$ K. Colors and symbols are as in figure 4.

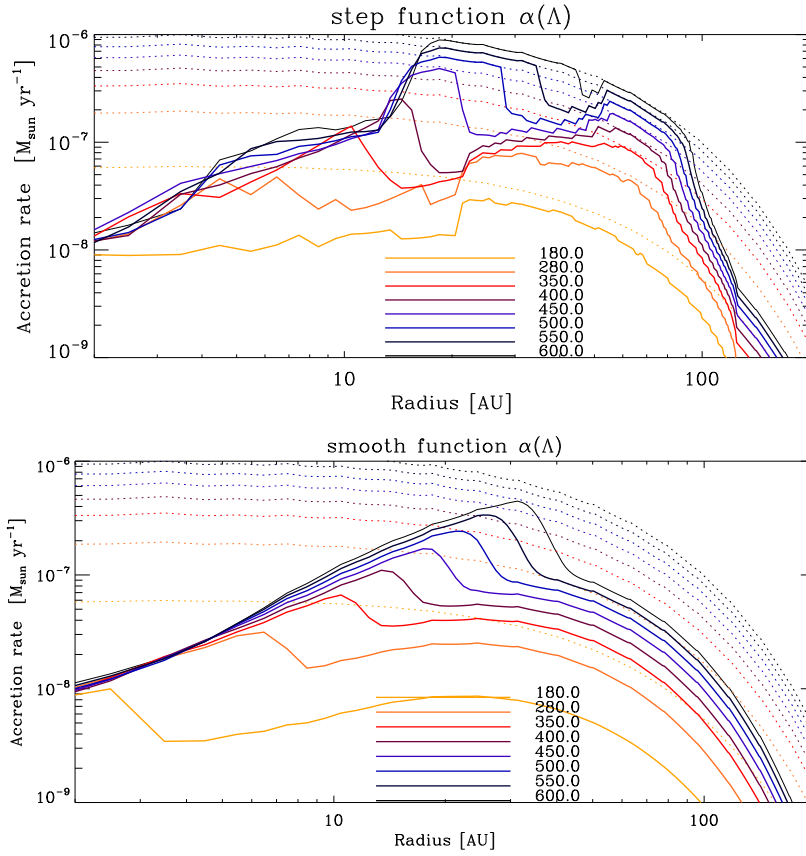


Fig. 18.— Accretion rate vs. radius in disks with various temperature profiles $T = T_0(r/1AU)^{-0.5}$ where $T_0 = 180, \dots, 600$ K. Dotted lines indicate the accretion rates when the whole disk is active.

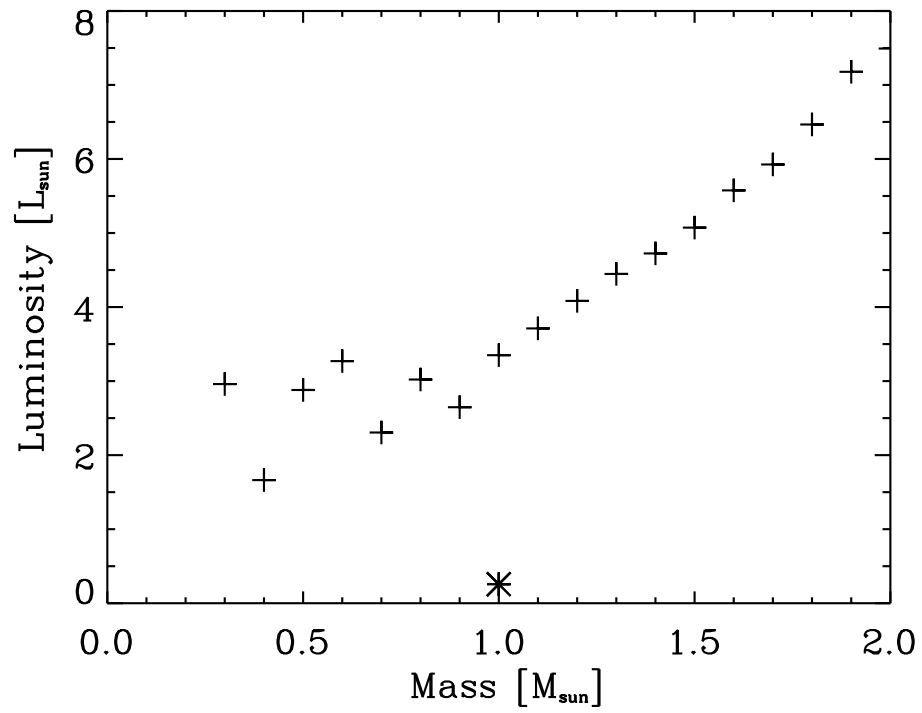


Fig. 19.— Stellar luminosity vs. stellar mass from evolutionary tracks at 1 Myr. A star symbol indicates the stellar luminosity in our fiducial model.

again islands of transitional coupling, located about $2H$ above and below the midplane (see section 4.7). The threshold between Mg^+ and HCO^+ makes itself visible in the shape of the MRI-active region’s outer border too. For the disks around stars from 1.2 to $2 M_\odot$, one can clearly see the MRI-active Mg^+ region overlapping with the HCO^+ region (bottom panels in Fig. 20). Interestingly, while the Mg^+ -dominated layers extend further out around heavier stars (see for example the $\Lambda = 10$ contours), the ambipolar term still beats out the induction term at $r > 40\text{AU}$ and $3 > (\Theta - \pi/2)/c_0 > 2$. As this effect occurs outside the exponential surface density cut-off, where the density falls rapidly with radius, we expect this would have little effect on the accretion rate.

The disks around the lower-mass stars have larger aspect ratios H/R or c_s/u_{Kep} . The Keplerian velocity u_{Kep} increases faster with the stellar mass than does the sound speed. Since we fix the ratio of disk to star mass, the surface density increases with the mass of the central object. This leads to larger dead zones in the more massive disks. We observe in Fig. 20 that indeed the disks around the higher-mass stars have smaller MRI-active regions. The separation between the inner and outer radial boundaries of the transitional layer on the midplane changes slowly with the stellar mass, being [6, 9, 10, 11, 12, 13] AU around stars of [0.4, 0.8, 1, 1.2, 1.6, 2] M_\odot . Thus over the stellar mass range, the transitional layer widens from 6 to 10 AU, while the transitional layer’s inner edge ($\log(\Lambda) = -1$ contour, or yellow-to-orange transition in Fig. 20) moves outward by 4 AU. For each stellar mass the accretion rate peaks near the Mg^+ freeze-out radius, beyond which the outer disk is less strongly accreting, considering the smooth dependence of the stress parameter on the Elsasser number (Fig. 21, bottom).

4.10. Cosmic Rays

The final parameter we vary is the cosmic ray ionization rate. We consider values 10, 100 and 1000 times greater than in the fiducial model (set 7, Table 2). A wide range of cosmic ray ionization rates is inferred from models of interstellar chemistry, and observations of HD, OH, D and especially H_3^+ and He^+ ions indicate rates up to $\zeta_{CR0} = 1.2 \times 10^{-15} \text{ s}^{-1}$ in the diffuse interstellar medium (Spitzer & Tomasko 1968; Webber 1998; van Dishoeck & Black 1986; Le Petit et al. 2004; Federman et al. 1996; Indriolo et al. 2007; McCall et al. 2003b; Indriolo et al. 2009). The distance to the galactic ridge is also important (Melia & Fatuzzo 2011).

From Fig. 22 we see that ambipolar diffusion loses much of its impact at a cosmic ray ionization rate of $10^{-16} - 10^{-15} \text{ s}^{-1}$. In the most extreme case, the Ohmic and ambipolar dead zones coincide. We also varied the dust-to-gas ratio, monomer size and surface density power-law index for a cosmic ray ionization rate of $5 \times 10^{-17} \text{ s}^{-1}$ (not shown here). The ambipolar diffusion still determines the dead zone outer edge location and the width of the transitional region. A sharp outer edge was proposed as a potential pressure trap for solid material in Lyra et al. (2009); Hasegawa & Pudritz (2010b,a). For high cosmic ray ionization rates (two bottom panels in Fig. 22), a large region with Elsasser number greater than 10 appears. We have a large volume with nearly ideal MHD conditions. However, the width of the transitional region is still 1-2 AU, seen from the radial

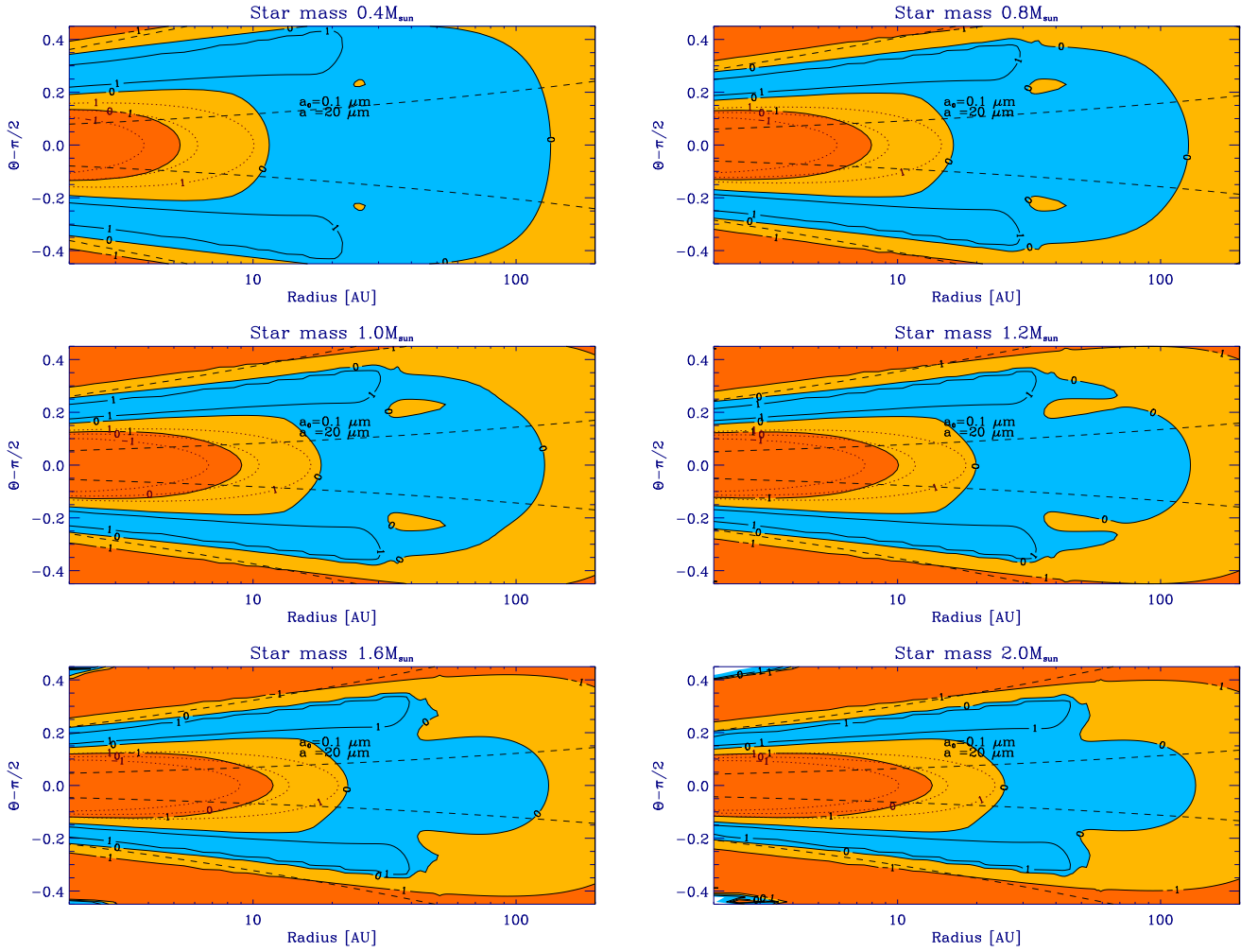


Fig. 20.— MRI-active region appearance for stars of various masses, with luminosities corresponding to age 1 Myr. Colors and symbols are as in figure 4.

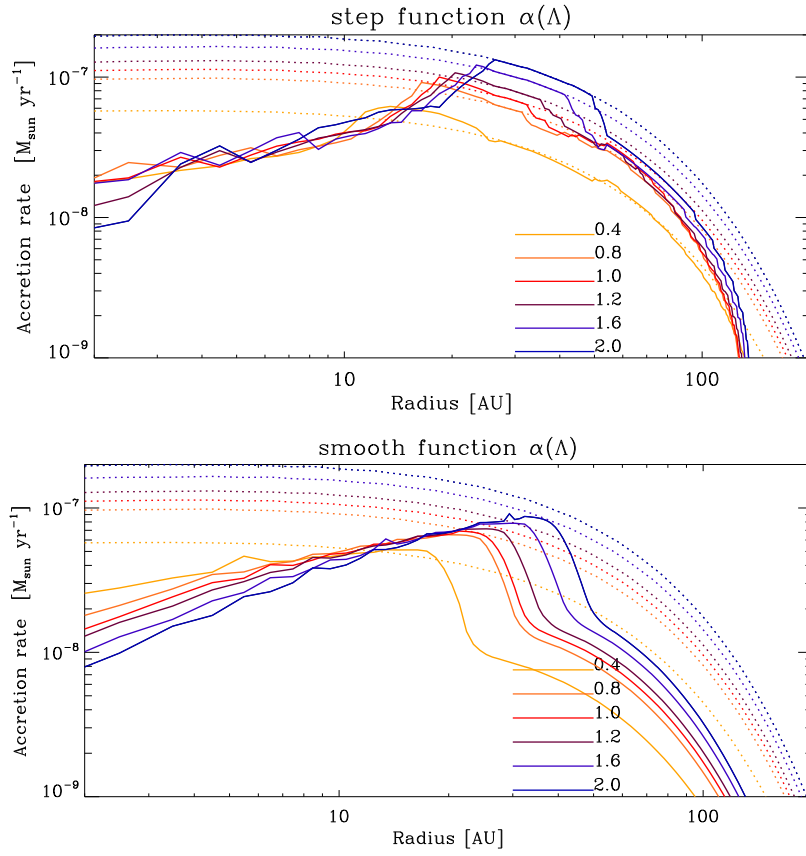


Fig. 21.— Accretion rate radial profiles in disks around stars with masses from 0.4 to $2 M_{\odot}$. Dotted lines indicate the profiles when the whole disk is active.

separation of the Elsasser number contour lines. The corresponding accretion rates for step-function and for smooth function in $\alpha(\Lambda)$ are shown in Fig. 23. In the case of smooth $\alpha(\Lambda)$, there is a peak in accretion rate at 8 AU visible for all models in set 7. At the inner disk boundary, \dot{M} increases from 10^{-8} to $10^{-7}M_{\odot}\text{yr}^{-1}$.

5. Discussion

Time Evolution of the Dead Zone: Over the lifetime of a protostellar disk, changes are likely in the dust-to-gas ratio f_{dg} as solid material is incorporated into planetesimals and planets. Let us consider the possibility that the dust evolves down two paths simultaneously. Most of the aggregates remain in place, while a fraction grows in mass through mutual collisions that are “lucky”, fast enough to overcome electrostatic forces and be compacted, but slow enough to avoid disruption. If the monomers’ size distribution remains unchanged, the fluffy aggregates’ mass fraction relative to the gas will decline with time, causing the dead zone to shrink and change shape. In Fig. 24 left panel we show schematically how the dead, transitional and active regions change their midplane radial extent with time, and so with decreasing dust-to-gas ratio. Time increases upward and is labeled in arbitrary units. The picture is made more complicated by the shorter timescales for evolution near the star.

In our first set of models we studied the impact of the monomer size a_0 on the ionization state. Real aggregates surely contain monomers with a distribution of sizes, possibly resembling the interstellar grain size distribution $n(a) \propto a^{-3.5}$ (Mathis et al. 1977). Accounting for the size distribution would likely make the Hall effect stronger at intermediate gas densities (Wardle & Ng 1999). Future work should clarify how the dispersion in a_0 in combination with the radius-dependent dust-to-gas ratio changes the dead zone’s shape.

The models in sets 3 and 4 show how changing disk mass and surface density shift the active zone inward or outward. In Fig. 24, dashed lines represent the correction to the dead and active zone borders when the density slope (or disk mass) changes at the same time the dust-to-gas ratio is decreasing. As the outer disk loses mass, the active zone expands inward (compare blue solid and dashed lines). The dead zone is situated in the inner part of the disk, where mass is gained slowly over time due to the weakness of the MRI-activity in the outer disk. For low dust-to-gas ratio, a second MRI-active zone appears inside 10 AU. We expect the accretion flow to drain mass from this new zone faster than mass is re-supplied from the outer parts. The surface density may be reduced locally, leading to a valley in the surface density. Over the long term the valley in surface density near the metal line will grow, becoming better and better ionized and leading to still higher accretion rates locally. If this process runs away, it could clear the inner disk of material. The right panel in Fig. 24 shows the expected time evolution of the surface density. Please note that Fig. 24 is a schematic representation. A more precise picture requires quantitative disk evolution models.

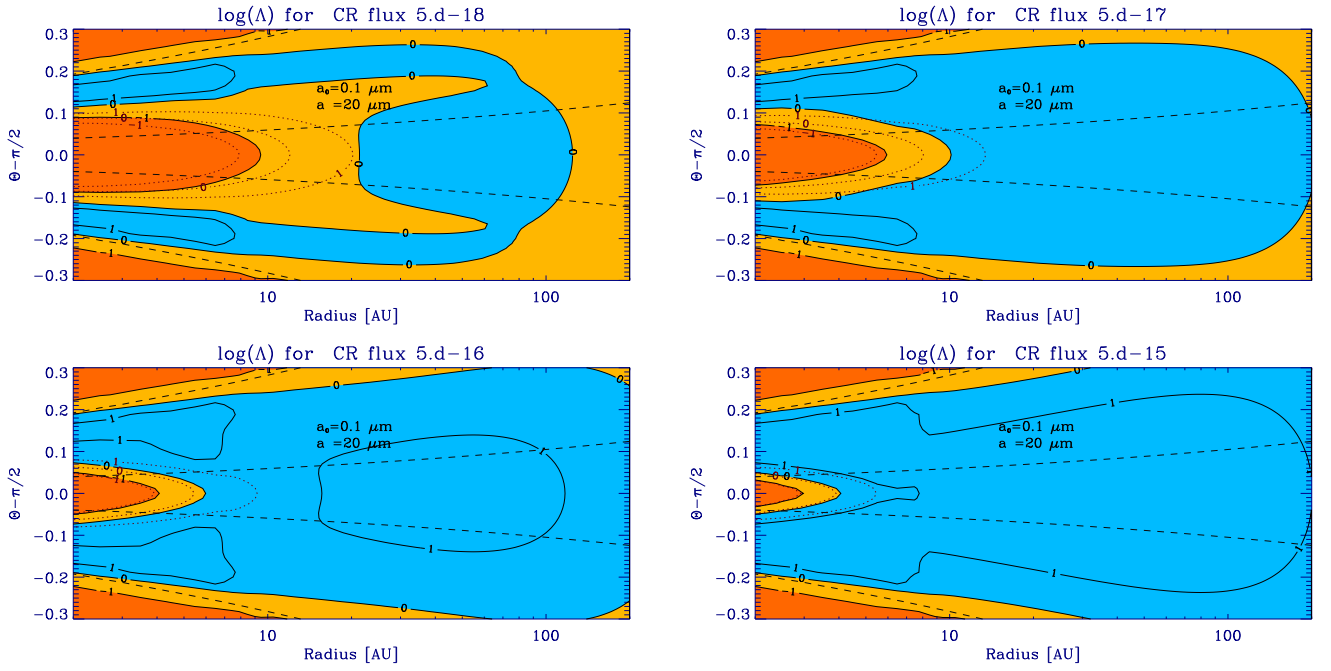


Fig. 22.— Dead, transitional and active zones with the cosmic ray ionization rate varying from $5 \times 10^{-18} \text{ s}^{-1}$ to $5 \times 10^{-17} \text{ s}^{-1}$, $5 \times 10^{-16} \text{ s}^{-1}$ and $5 \times 10^{-15} \text{ s}^{-1}$. Colors and symbols are as in figure 4.

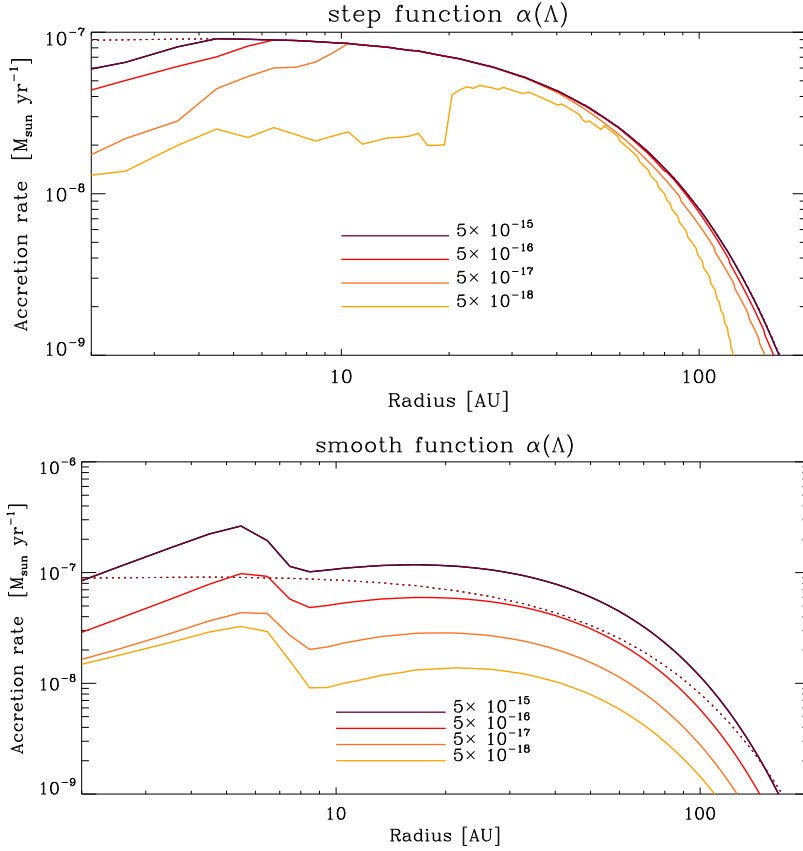


Fig. 23.— Accretion rates vs. radius in set 7 with cosmic ray fluxes at the disk surface from 5×10^{-18} to 5×10^{-15} . The dotted line indicates the profile when the whole disk is active. Note that the smooth dependence of turbulent stress on Elsasser number leads to higher accretion rates in the $\Lambda > 10$ regions (see section 3.2).

Dependence of the Stress on Elsasser Number: Gaps appear in the accretion rate’s radial profile in many cases when we assume the stress parameter α is a step function across Elsasser number unity (figures 10, 14, 18). A step function adequately approximates the turbulent stress’ variation with height in the inner disk, where conductivity gradients are steep. The step function is harder to justify when modeling the radial variation in the outer disk, however. We demonstrated here that the outer disk can have a quite different accretion rate profile if $\alpha(\Lambda)$ is a smooth function. The reason is that the Elsasser number is near unity over a large range of radii $r > 10$ AU. Thus much of the outer disk is marginally MRI-active.

We assume a field strength such that the magnetic pressure is a fixed fraction of the midplane gas pressure at each radius. A more complete approach would involve making the stress proportional to the magnetic pressure in the saturated turbulence. Bai (2011) provides a fitting function for the minimum possible plasma beta of the saturated fields in the presence of ambipolar diffusion. We have constructed the corresponding turbulent stress profile (not shown in this paper), applying the floor for plasma beta mentioned above. It is reassuring that the radial profiles of the accretion rate are basically the same as those we present here. When compared to the accretion rates derived from $\alpha \propto 1/\beta$, the accretion is faster near the inner radial boundary using Bai’s fit, because the weaker magnetic fields leave more of the upper layers with $\beta < 1$. This deserves to be investigated in more detail using 3-D MHD simulations of MRI turbulence including both Ohmic and ambipolar diffusion.

Accretion Variability: It is noteworthy that all models show an accretion rate peak just inside the metal line, which lies at 8 AU in our fiducial model. This radial location is affected by the disk temperature. The temperature thus affects the location and shape of the MRI-active zone.

The luminosity produced by the typical T Tauri accretion rate $10^{-8}M_{\odot}/\text{yr}$ on a star of Solar mass and 2 Solar radii is $GMM_{\odot}/r \sim 0.1L_{\odot}$, probably not enough to significantly change temperatures inside the disk region we consider. However during FU Orionis outbursts, the accretion luminosity rises sufficiently to increase the overall system brightness a hundredfold (Hartmann & Kenyon 1996), requiring disk temperatures to at least triple. This is likely to expand the Mg^+ -dominated region. The outbursts last about 100 years, a few orbits at 10 AU in our fiducial model and long enough for MRI turbulence to reach saturation in the newly-coupled gas. Thus we expect the peak in the accretion rate to move to larger radii as in set 5.

Limitations: The outer radial border of the MRI-active zone coincides with the gas density contour $10^{-15} \text{ g cm}^{-3}$, lying at 128 AU in our fiducial model (section 4.1). Since gas-phase molecular reactions dominate the recombination outside 100 AU, it would be useful to recalculate the ion and electron densities there using the extended chemical network, in order to validate our findings on the ambipolar diffusion.

Additionally, our chemical network includes only one representative metal, magnesium, but of

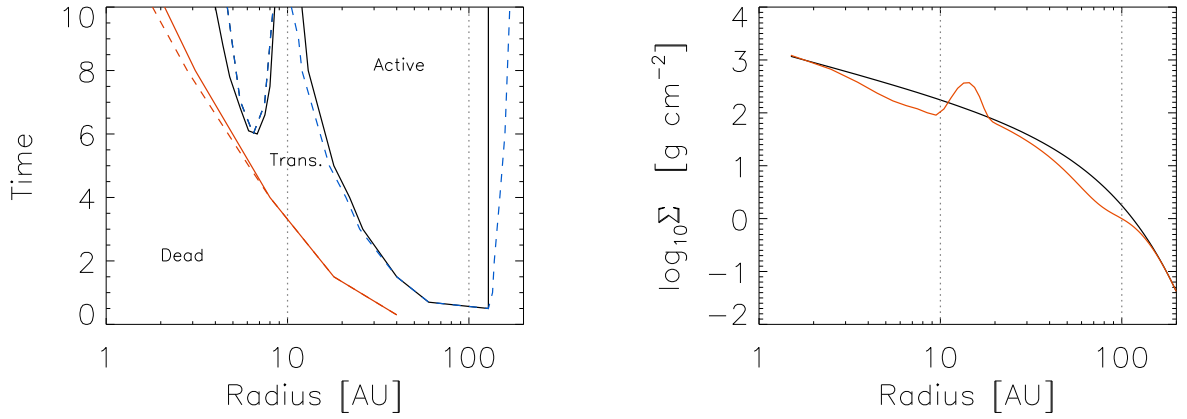


Fig. 24.— Left: Schematic picture of the time evolution of the dead, transitional and active regions. Solid lines show the regions’ borders when only the dust-to-gas ratio is allowed to decrease with time. Dashed lines include corrections for the gas surface density and disk mass evolving simultaneously. Right: The black line shows the surface density in our fiducial model. The red line shows the expected evolution to form a local gas pressure maximum capable of trapping solid bodies near the metal line (8 AU), surrounded by valleys in the surface density which will be better-ionized and potentially MRI-active.

course many metals can occur in the gas phase, and each has its own thermal desorption temperature. There should then be multiple metal lines, one for the freeze-out of each metal.

All the metal lines will shift when we consider a more detailed temperature distribution. In our simple model the temperature is constant on cylinders, an approximation which is appropriate only for the disk’s optically thick interior. The surface layers are typically hotter because they are directly illuminated by the starlight (Dullemond et al. 2007), so the metal lines would bend away from the star with increasing distance from the equatorial plane.

We may also ask whether a steeper radial variation in the Elsasser number can be obtained with a radial gradient in, for example, dust-to-gas ratio or grain charging properties. A steeper $\Lambda(r)$ would yield bigger differences in the stresses between the transitional, dead and MRI-active zones. Such variations also open the possibility of planetesimal traps at multiple radii.

6. Conclusions

We determine dead zone sizes and shapes in disks where the ionization state is controlled by recombination on fluffy dust aggregates. We study the effects of parameters including the constituent monomer size, the aggregates’ mass fraction, the magnetic field strength, the masses of the disk and star, the slope of the surface density profile, the disk temperature and the cosmic ray ionization rate. The three parameters most strongly affecting the dead zone are the monomer size, the dust mass fraction and the cosmic ray rate.

We find that ambipolar diffusion generally defines the dead zone’s outer radial boundary, as well as the thickness of the transitional layer just inside the boundary. The ambipolar diffusion is overridden by Ohmic dissipation near the dead zone edge only if the magnetic fields are weak enough that the midplane plasma beta is greater than 4000, corresponding to field strengths $B < 0.15$ mGauss at 100 AU.

The fractal aggregates are efficient in sweeping up free electrons and ions, providing a major recombination pathway at gas densities greater than 10^{-14} gcm^{-3} . Nevertheless the disk surface layers couple to the magnetic fields sufficiently for MRI turbulence to drive accretion. Accurately estimating the resulting mass flow rates requires carefully treating the stresses’ dependence on the Elsasser number. A step function is an inadequate description because so much of the disk has Elsasser numbers near the critical value. The mass flow is 10^{-9} – $10^{-8} M_{\odot} \text{yr}^{-1}$ at 1 AU for our fiducial cosmic ray ionization rate of $5 \times 10^{-18} \text{ s}^{-1}$. This is similar to the findings of Bai (2011), who considered compact grains rather than fractal aggregates.

The dead zone’s outer edge, which we call the transitional region and define by Elsasser numbers from 0.1 to 1, is generally very broad at the midplane. Its width is 12 AU in our fiducial model and ranges from 2 AU in our most strongly-ionized model from set 7, to the entire disk at the maximum dust-to-gas ratio from set 1. The mass flow rates indicate that the transitional region

will accumulate no sharp density bump as the disk evolves. On the other hand we find that the magnetic coupling, and therefore the flow rate, declines steeply where the temperature falls below a threshold allowing metal atoms to thermally adsorb on the grains. Such a metal freeze-out can cause a local maximum in the flow rate, leading to a gap in the surface density with a long-lived pileup of material just outside. This kind of accretion peak occurs in all models across the parameter study, shifting in radius according to the disk temperature distribution.

By varying each of the parameters in turn, we find:

- At dust aggregate mass fractions near 10^{-2} , thin MRI-active surface layers yield mass flow rates $10^{-9} M_{\odot}\text{yr}^{-1}$. At mass fractions below 10^{-4} the dead zone takes a fish-tail shape in meridional cross-section, and the mass flow rate is around $10^{-8} M_{\odot}\text{yr}^{-1}$. Even at very low dust concentrations, there is a patch at $r \gtrsim 10$ AU where the magnesium atoms freeze out and ambipolar diffusion pushes the Elsasser number into the transitional regime $0.1 < \Lambda < 1$.
- The monomer size also affects the dead zone shape. When the monomers are 10 nm or smaller, giving the aggregates a large cross-section for a given solid mass, the activity is confined to narrow isolated surface layers along with a blob of marginally active gas near 100 AU. When the monomers are 100 nm or larger, the dead zone takes the fishtail shape.
- Varying the surface density slope or the disk mass reveals the dead zone’s origins. With increasing disk mass we observe larger MRI-active zones in the outer parts, as higher densities lead to more frequent collisions with neutrals, thwarting ambipolar diffusion. A similar effect comes from reducing the surface density slope so that more of the mass resides far from the star. The dead zone’s outer edge lies at 20 AU for disk masses between 0.5 and 1.5 times the fiducial model. At surface density slopes 1.3 and steeper, ambipolar diffusion isolates a midplane marginally-active region outside 20 AU.
- Making the disk hotter or colder also changes the dead zone’s shape. The fishtail appears when the magnesium freezeout line lies near the inner edge of the annulus where ambipolar diffusion at intermediate heights separates magnetically-active layers in the better-ionized surface and denser interior.
- The dead zone’s dependence on stellar mass combines the impacts of disk mass, gravity and temperature. For our chosen stellar masses and ages (0.4 to $2 M_{\odot}$, all at 1 Myr), the disks are so hot that the Mg^+ -dominated region extends far from the star and no fishtail deadzone appears. Both the magnesium freezeout line and the corresponding accretion rate peak are shifted to larger radii with increasing stellar mass. The magnesium line ranges from 10 to 25 AU over the stellar mass range we consider.

We identify a new way to create a local pressure maximum capable of trapping solid particles. The steep gradient in mass flow rate across the metal freezeout line means the magnetic stresses will evacuate the side of the line near the star, while material piles up beyond. Gas drag forces from

headwinds outside the maximum, and tail winds inside, will bring solid particles toward the peak. The radial gradients could grow strong enough to trigger the formation of vortices, contributing to angular momentum transport in the weakly magnetically coupled transitional region (Flock et al. 2012; Raettig et al. 2012) and further concentrating solid material. Testing the effectiveness of such traps is a challenging task. Probing the distribution of the field strength in the MRI turbulence requires global 3-D MHD simulations with ambipolar diffusion. Ionization chemistry and the metal freezeout must be treated. The pressure profile’s evolution near the metal line over the longer accretion timescales might be explored using azimuthally-averaged mass transport calculations with turbulent stresses obtained from MHD simulations. Since the MRI turbulence and dust are mutually coupled and feedback is possible, an important part of the story will be the evolving dust abundance and the corresponding changes in the shape of the dead zone.

N. Dzyurkevich was supported by the Deutsche Forschungsgemeinschaft (DFG) through Forschergruppe 759, “The Formation of Planets: The Critical First Growth Phase”. We acknowledge support from the Deutsches Zentrum für Luft- und Raumfahrt (DLR), support code 50 OR 0401. N. J. Turner’s participation was supported by the NASA Solar Systems Origins program under grant 07-SSO07-0044, and by the Alexander von Humboldt Foundation through a Fellowship for Experienced Researchers. The work was carried out in part at the Jet Propulsion Laboratory, California Institute of Technology. We thank Prof. W. Brandner and M. Gennaro for the tutoring on the STELLAR code. We thank S. Okuzumi for a very thorough referee report that greatly improved the quality of this paper.

REFERENCES

- Andrews, S. M., Wilner, D. J., Hughes, A. M., Qi, C., & Dullemond, C. P. 2009, *ApJ*, 700, 1502
- Armitage, P. J., Livio, M., & Pringle, J. E. 2001, *MNRAS*, 324, 705
- Bai, X.-N. 2011, *ApJ*, 739, 51
- Bai, X.-N., & Goodman, J. 2009, *ApJ*, 701, 737
- Bai, X.-N., & Stone, J. M. 2011, *ApJ*, 736, 144
- Balbus, S. A., & Hawley, J. F. 1991, *ApJ*, 376, 214
- . 1998, *Reviews of Modern Physics*, 70, 1
- Beck, R., Brandenburg, A., Moss, D., Shukurov, A., & Sokoloff, D. 1996, *ARA&A*, 34, 155
- Beck, R., & Hoernes, P. 1996, *Nature*, 379, 47
- Blaes, O. M., & Balbus, S. A. 1994, *ApJ*, 421, 163

- Blum, J. 2004, in *Astronomical Society of the Pacific Conference Series*, Vol. 309, *Astrophysics of Dust*, ed. A. N. Witt, G. C. Clayton, & B. T. Draine, 369
- Blum, J., & Wurm, G. 2000, *Icarus*, 143, 138
- Blum, J., Wurm, G., Poppe, T., & Heim, L.-O. 1998, *Earth Moon and Planets*, 80, 285
- Bodenheimer, P., Laughlin, G. P., Różyczka, M., & Yorke, H. W., eds. 2007, *Numerical Methods in Astrophysics: An Introduction*
- Bouwman, J., Meeus, G., de Koter, A., et al. 2001, *A&A*, 375, 950
- Brandenburg, A., Nordlund, A., Stein, R. F., & Torkelsson, U. 1995, *ApJ*, 446, 741
- Brauer, F., Henning, T., & Dullemond, C. P. 2008, *A&A*, 487, L1
- Chiang, E. I., & Goldreich, P. 1997, *ApJ*, 490, 368
- Cowling, T. G. 1976, *Magnetohydrodynamics* (Monographs on Astronomical Subjects, Bristol: Adam Hilger, 1976)
- Desch, S. J. 2004, *ApJ*, 608, 509
- Dominik, C., Blum, J., Cuzzi, J. N., & Wurm, G. 2007, *Protostars and Planets V*, 783
- Draine, B. T., Roberge, W. G., & Dalgarno, A. 1983, *ApJ*, 264, 485
- Dullemond, C. P., Hollenbach, D., Kamp, I., & D’Alessio, P. 2007, *Protostars and Planets V*, 555
- Dzyurkevich, N., Flock, M., Turner, N. J., Klahr, H., & Henning, T. 2010, *A&A*, 515, A70
- Federman, S. R., Weber, J., & Lambert, D. L. 1996, *ApJ*, 463, 181
- Flaig, M., Ruoff, P., Kley, W., & Kissmann, R. 2012, *MNRAS*, 420, 2419
- Fleming, T., & Stone, J. M. 2003, *ApJ*, 585, 908
- Flock, M., Dzyurkevich, N., Klahr, H., Turner, N., & Henning, T. 2012, *ApJ*, 744, 144
- Flock, M., Dzyurkevich, N., Klahr, H., Turner, N. J., & Henning, T. 2011, *ApJ*, 735, 122
- Fromang, S., & Nelson, R. P. 2006, *A&A*, 457, 343
- Furlan, E., Watson, D. M., McClure, M. K., et al. 2009, *ApJ*, 703, 1964
- Gammie, C. F. 1996, *ApJ*, 457, 355
- Glassgold, A. E., Najita, J., & Igea, J. 1997, *ApJ*, 480, 344
- Guan, X., & Gammie, C. F. 2011, *ApJ*, 728, 130

- Hartmann, L., Calvet, N., Gullbring, E., & D’Alessio, P. 1998, *ApJ*, 495, 385
- Hartmann, L., & Kenyon, S. J. 1996, *ARA&A*, 34, 207
- Hasegawa, T. I., Herbst, E., & Leung, C. M. 1992, *ApJS*, 82, 167
- Hasegawa, Y., & Pudritz, R. E. 2010a, *ApJ*, 710, L167
- . 2010b, *MNRAS*, 401, 143
- . 2011, *MNRAS*, 417, 1236
- Hawley, J. F., Gammie, C. F., & Balbus, S. A. 1995, *ApJ*, 440, 742
- Hawley, J. F., & Stone, J. M. 1998, *ApJ*, 501, 758
- Hirose, S., & Turner, N. J. 2011, *ApJ*, 732, L30
- Hughes, A. M., Wilner, D. J., Qi, C., & Hogerheijde, M. R. 2008, *ApJ*, 678, 1119
- Igea, J., & Glassgold, A. E. 1999, *ApJ*, 518, 848
- Ilgner, M., & Nelson, R. P. 2006, *A&A*, 445, 223
- Indriolo, N., Fields, B. D., & McCall, B. J. 2009, *ApJ*, 694, 257
- Indriolo, N., Geballe, T. R., Oka, T., & McCall, B. J. 2007, *ApJ*, 671, 1736
- Johansen, A., Klahr, H., & Henning, T. 2011, *A&A*, 529, A62
- Johansen, A., & Youdin, A. 2007, *ApJ*, 662, 627
- Johansen, A., Youdin, A., & Klahr, H. 2009, *ApJ*, 697, 1269
- Kempf, S., Pfalzner, S., & Henning, T. K. 1999, *Icarus*, 141, 388
- Kim, W.-T., & Ostriker, E. C. 2000, *ApJ*, 540, 372
- Krejny, M., Matthews, T. G., Novak, G., et al. 2009, *ApJ*, 705, 717
- Kretke, K. A., & Lin, D. N. C. 2007, *ApJ*, 664, L55
- Kunz, M. W., & Balbus, S. A. 2004, *MNRAS*, 348, 355
- Le Petit, F., Roueff, E., & Herbst, E. 2004, *A&A*, 417, 993
- Lyra, W., Johansen, A., Zsom, A., Klahr, H., & Piskunov, N. 2009, *A&A*, 497, 869
- Mac Low, M.-M., Norman, M. L., Konigl, A., & Wardle, M. 1995, *ApJ*, 442, 726
- Martin, R. G., & Livio, M. 2012, *MNRAS*, 425, L6

- Martin, R. G., Lubow, S. H., Livio, M., & Pringle, J. E. 2012, MNRAS, 423, 2718
- Mathis, J. S., Ruml, W., & Nordsieck, K. H. 1977, ApJ, 217, 425
- McCall, B. J., Huneycutt, A. J., Saykally, R. J., et al. 2003a, Nature, 422, 500
- . 2003b, Nature, 422, 500
- Meakin, P. 1991, Reviews of Geophysics, 29, 317
- Melia, F., & Fatuzzo, M. 2011, MNRAS, 410, L23
- Miller, K. A., & Stone, J. M. 2000, ApJ, 534, 398
- Muranushi, T., Okuzumi, S., & Inutsuka, S.-i. 2012, ApJ, 760, 56
- Okuzumi, S. 2009, ApJ, 698, 1122
- Okuzumi, S., & Hirose, S. 2011, ApJ, 742, 65
- Perez-Becker, D., & Chiang, E. 2011, ApJ, 727, 2
- Pinilla, P., Birnstiel, T., Ricci, L., et al. 2012, A&A, 538, A114
- Raettig, N., Lyra, W., & Klahr, H. 2012, ArXiv e-prints
- Sano, T., Inutsuka, S.-i., Turner, N. J., & Stone, J. M. 2004, ApJ, 605, 321
- Sano, T., & Miyama, S. M. 1999, ApJ, 515, 776
- Sano, T., Miyama, S. M., Umebayashi, T., & Nakano, T. 2000, ApJ, 543, 486
- Sano, T., & Stone, J. M. 2002a, ApJ, 570, 314
- . 2002b, ApJ, 577, 534
- Semenov, D., Wiebe, D., & Henning, T. 2004, A&A, 417, 93
- Simon, J. B., Bai, X.-N., Stone, J. M., Armitage, P. J., & Beckwith, K. 2012, ArXiv e-prints
- Simon, J. B., Hawley, J. F., & Beckwith, K. 2009, ApJ, 690, 974
- Spitzer, Jr., L., & Tomasko, M. G. 1968, ApJ, 152, 971
- Suyama, T., Wada, K., & Tanaka, H. 2008, ApJ, 684, 1310
- Tout, C. A., & Pringle, J. E. 1992, MNRAS, 259, 604
- Turner, N. J., Carballido, A., & Sano, T. 2010, ApJ, 708, 188
- Turner, N. J., & Drake, J. F. 2009, ApJ, 703, 2152

- Turner, N. J., & Sano, T. 2008, *ApJ*, 679, L131
- Umeybayashi, T. 1983, *Progress of Theoretical Physics*, 69, 480
- Umeybayashi, T., & Nakano, T. 1981, *PASJ*, 33, 617
- . 2009, *ApJ*, 690, 69
- Uribe, A. L., Klahr, H., Flock, M., & Henning, T. 2011, *ApJ*, 736, 85
- van Dishoeck, E. F., & Black, J. H. 1986, *ApJS*, 62, 109
- Wardle, M. 2007, *Ap&SS*, 311, 35
- Wardle, M., & Ng, C. 1999, *MNRAS*, 303, 239
- Wardle, M., & Salmeron, R. 2012, *MNRAS*, 422, 2737
- Webber, W. R. 1998, *ApJ*, 506, 329
- Weidenschilling, S. J., & Cuzzi, J. N. 1993, in *Protostars and Planets III*, ed. E. H. Levy & J. I. Lunine, 1031–1060
- Wolk, S. J., Harnden, Jr., F. R., Flaccomio, E., et al. 2005, *ApJS*, 160, 423
- Wurm, G., & Blum, J. 1998, *Icarus*, 132, 125
- Zhu, Z., Hartmann, L., & Gammie, C. 2010, *ApJ*, 713, 1143

A. Determining Gas-Phase Metal Abundance

Most of the metal atoms are incorporated into grains. The remainder can occur either free in the gas, where they are available to participate in the ionization balance, or adsorbed on grain surfaces. We determine here the number density of the metal atoms in the gas phase, which depends on temperature. We consider only the atoms’ thermal adsorption on and desorption from the grains. Gas-phase species X when captured on the grains is labeled gX . The equilibrium number density on the grains is given by

$$n[gX] = \frac{k_1 S_x}{k_2} n[X] n_{\text{gr}} = an[X], \quad (\text{A1})$$

where the coefficients $k_1 = \sigma_{\text{gr}} v_{\text{th}}$ and k_2 are adsorption and desorption rates. The number density in the gas

$$n[X] = n[X]^{\text{total}} - n[gX]. \quad (\text{A2})$$

We determine the amount of magnesium on the grain surfaces using the expression

$$n[g\text{Mg}] = a \frac{n[\text{Mg}]^{\text{total}}}{1 + a}, \quad (\text{A3})$$

and in the gas phase

$$n[\text{Mg}] = \frac{n[\text{Mg}]^{\text{total}}}{1 + a}. \quad (\text{A4})$$

The initial abundances are 1 for H₂, 9.75×10^{-2} for He, 3.62 and 8.53×10^{-4} for C and O, and 1×10^{-11} for Mg (Ilgner & Nelson 2006). Not every collision with a grain leads to sticking, and the sticking probability is $S_X = \exp(-E_{kin}/\sqrt{(2E_D\Delta E_{trans})})$, with $\Delta E_{trans} \simeq 2 \times 10^{-3}$ eV for the energy transfer to the grain via lattice vibrations. $E_D^{\text{H}_2} = 450$, $E_D^{\text{HCO}^+} = 1510$ and $E_D^{\text{Mg}} = 5300 k_B$ K. The desorption coefficient $k_2 = \nu_0 \exp(-E_D/kT)$ with $\nu_0 = \sqrt{(3 \times 10^{15} \text{cm}^{-2} E_D / (\pi^2 m_x))}$ (Hasegawa et al. 1992). After finding the gas-phase metal abundance, we compute the total recombination rate c_t for the dominant ion by applying an iterative approach (section 2.4).

B. Gaussian Charge State Distribution – Limit of Validity

We find the abundances of the ions, electrons and charged grains from Okuzumi (2009) eqs. 32, 33 and 22, letting the grains charge by up to 30 electrons either side of their mean charge. The grains' charge state distribution is very well-approximated by the Gaussian when the grains carry many charges each. Small aggregates however charge weakly enough that their few discrete charge states can differ noticeably from a Gaussian. As a result the plasma is not quite charge-neutral overall. Fig. 25 demonstrates the accuracy of the charge neutrality for three different radii in the fiducial model. The largest errors occur near the midplane where most of the charge resides on the grains. Accuracy is good when the fluffy grains are made of $N > 400$ monomers, while relatively large departures from neutrality occur when $N < 10$. Several of the assumptions used by Okuzumi (2009) break down when the number of monomers is too small, including the assumption of negligible electric polarization. But most importantly, charge neutrality is violated when the grains' charge spread is too small to be represented with a Gaussian.

C. MRI Criterion When Ambipolar Diffusion Dominates

Whether MRI turbulence can operate under an ambipolar-dominated magnetic diffusivity is sometimes judged using the ion magnetic Reynolds number. In this Appendix we examine the general conditions for this number to be equivalent to the ambipolar Elsasser number. That is, we seek the requirements for $Re_i \approx \Lambda_A$ or

$$\frac{\gamma_i \rho_i}{\Omega} \approx \frac{v_A^2}{\eta_A \Omega} \quad (\text{C1})$$

or

$$\eta_A \approx \frac{B^2}{4\pi \rho \gamma_i \rho_i}. \quad (\text{C2})$$

Recall

$$\eta_A = \frac{c^2}{4\pi} \left(\frac{\sigma_P}{\sigma_\perp^2} - \frac{1}{\sigma_O} \right) \quad (\text{C3})$$

from eq. 27. Let each of the three conductivities be dominated by a single species. Label the main Ohmic species' mass m_O , charge q_O , number density n_O , collision coefficient γ_O and coupling parameter b_O , and similarly for the Hall and Pedersen conductivities:

$$\sigma_O = \frac{ec}{B} n_O q_O \left(\frac{eBq_O}{m_O c \gamma_O \rho} \right) \quad (\text{C4})$$

$$\sigma_H = \frac{ec}{B} \frac{n_H q_H}{1 + \left(\frac{eBq_H}{m_H c \gamma_H \rho} \right)^2} \quad (\text{C5})$$

$$\sigma_P = \frac{ec}{B} \frac{n_P q_P \left(\frac{eBq_P}{m_P c \gamma_P \rho} \right)}{1 + \left(\frac{eBq_P}{m_P c \gamma_P \rho} \right)^2} \quad (\text{C6})$$

We have used charge neutrality to derive eq. C5 from eq. 24. Notice that σ_O is independent of the field strength, so we can end up with $\eta_A \propto B^2$ as in eq. C2 only if the final term in eq. C3 is negligible.

Now the perpendicular conductivity $\sigma_\perp = \sqrt{\sigma_H^2 + \sigma_P^2}$ can be dominated by either σ_H or σ_P . We consider the two possibilities in turn. If $\sigma_H \gg \sigma_P$, the remaining piece of the right-hand side of eq. C3 is

$$\frac{\sigma_P}{\sigma_H^2} = \frac{n_P q_P^2}{m_P \gamma_P \rho} \left(\frac{B}{c n_H q_H} \right)^2 \left(1 + \left[\frac{eBq_P}{m_P c \gamma_P \rho} \right]^2 \right)^{-1} \left(1 + \left[\frac{eBq_H}{m_H c \gamma_H \rho} \right]^2 \right)^2. \quad (\text{C7})$$

This reduces to eq. C2 if three conditions are met:

1. The ions dominate the Pedersen conductivity.
2. The ions have the same number density and charge magnitude as the Hall species, i.e. $n_H = n_P = n_i$ and $|q_H| = |q_P| = |q_i|$. For example, the ions could also dominate the Hall conductivity.
3. Both the ions and the Hall species are poorly coupled, so $b_i = b_P \ll 1$ and $b_H \ll 1$ and the terms not quadratic in B can be neglected.

In the other case, where $\sigma_H \ll \sigma_P$, the right-hand side of eq. C3 becomes

$$\frac{1}{\sigma_P} = \left(n_P q_P^2 \frac{e^2}{m_P \gamma_P \rho} \right)^{-1} \left(1 + \left[\frac{eBq_P}{m_P c \gamma_P \rho} \right]^2 \right). \quad (\text{C8})$$

This reduces to eq. C2 if the ions again determine the Pedersen conductivity, and in addition the term proportional to B^2 dominates, i.e. the ions couple to the fields and $b_i = b_P \gg 1$.

We next look at how the Ohmic term becomes negligible in the ambipolar diffusivity when the other requirements for eq. C2 are met. In the first case, where $\sigma_H \gg \sigma_P$, the Ohmic term is small if $\sigma_O \gg \sigma_H^2/\sigma_P$ or

$$n_{OQO}b_O \gg \left(\frac{n_H^2 q_H^2}{n_P q_P} \right) \frac{1 + b_P^2}{b_P(1 + b_H^2)^2}. \quad (\text{C9})$$

Now in this first case, eq. C2 works only when conditions 1-3 are satisfied. Under the conditions, eq. C9 simplifies to

$$b_O \gg \frac{n_i q_i}{n_{OQO}} b_i^{-1}. \quad (\text{C10})$$

That is, the Ohmic species must not decouple too much from the magnetic fields. Throughout our fiducial model disk, and over a wide range of other models, the Ohmic conductivity comes from the electrons. Since these have the same charge magnitude as the ions, and a coupling parameter $b_e \approx 1000b_i$ due to their low mass, eq. C10 means the ion coupling must satisfy $1000b_i^2 \gg n_i/n_e$. Also the electrons have the same number density as the ions in the ion-electron plasma limit where grain-surface recombination is unimportant, while in the opposite limit of an ion-dust plasma the electrons' depletion onto grains yields $n_e \approx 10^{-2}n_i$ (eq. 38 of Okuzumi 2009). Eq. C10 then requires $b_i \gg 0.03$ and $b_i \gg 0.3$, respectively. These are incompatible or just barely compatible with $b_i \ll 1$ needed by condition 3. Eq. C2 is therefore valid at most in a narrow range of ion coupling parameters when $\sigma_H \gg \sigma_P$.

In the second case, where $\sigma_H \ll \sigma_P$, the Ohmic term can be dropped when $\sigma_O \gg \sigma_P$, that is when

$$n_{OQO}b_O \gg \frac{n_P q_P b_P}{1 + b_P^2}. \quad (\text{C11})$$

Since eq. C2 works in this case only if $b_P \gg 1$, it is enough to say the Ohmic term is small when

$$b_O \gg \frac{n_i q_i}{n_{OQO}} b_i^{-1}, \quad (\text{C12})$$

the same form as eq. C10. Even the stronger of the two constraints derived above for eq. C10, $b_i \gg 0.3$, is already met in this case by our requirement that $b_i = b_P \gg 1$.

Considering the two cases together, we see that the ion Reynolds number is equivalent to the ambipolar Elsasser number if the ions couple to the field and dominate the Pedersen conductivity, which in turn is larger than the Hall conductivity.

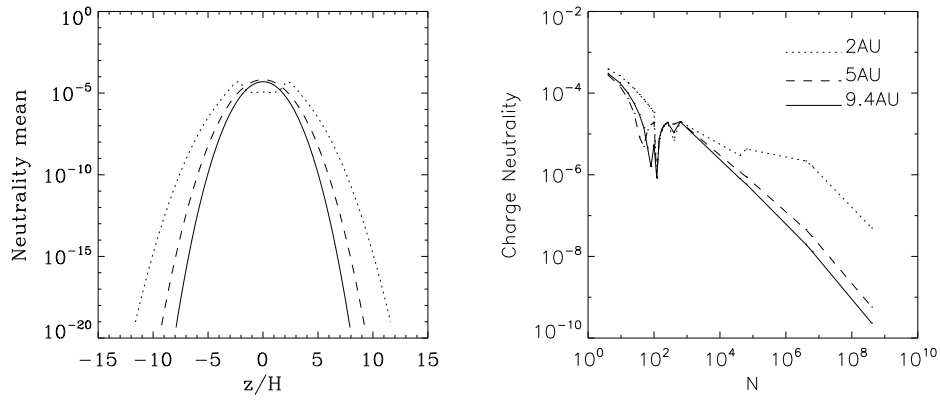
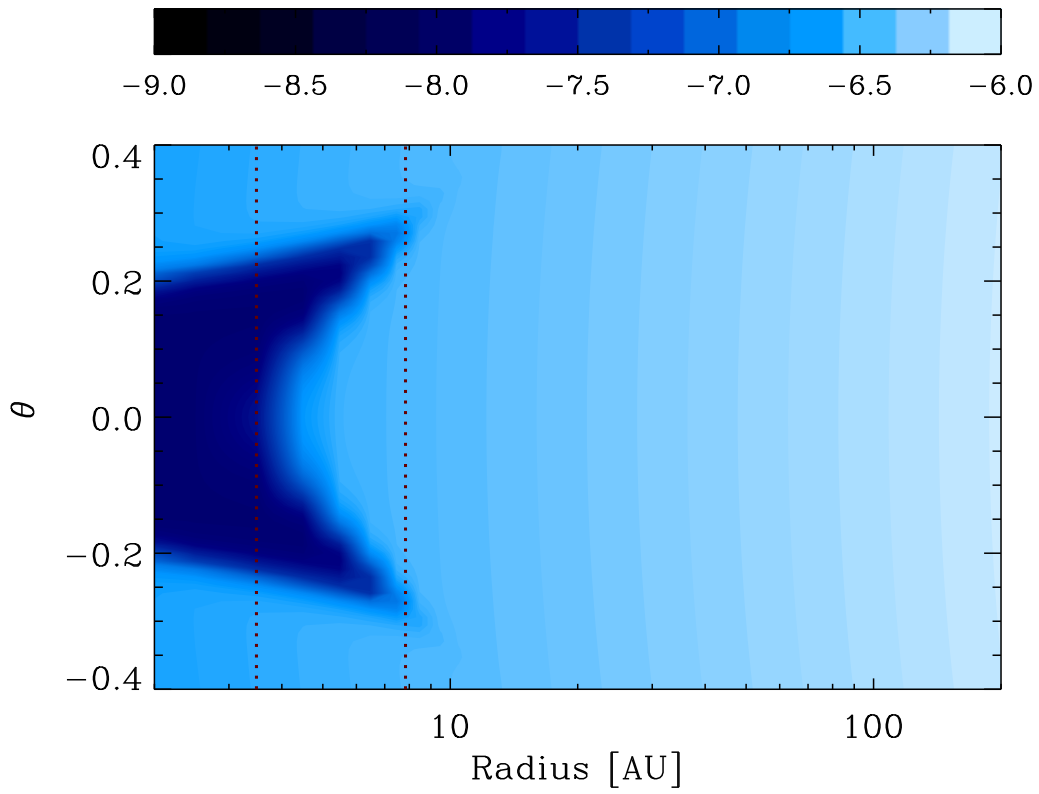
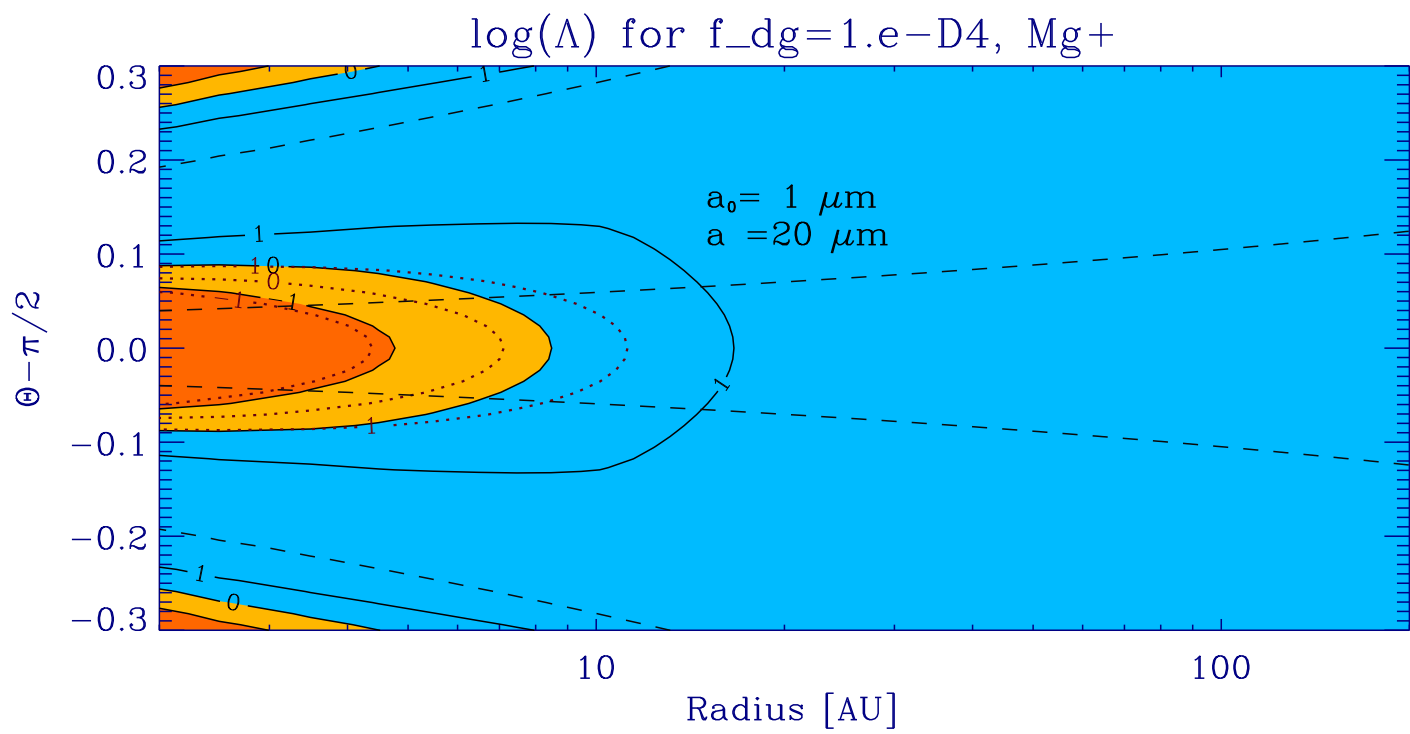


Fig. 25.— Left: Charge neutrality for $R = 2, 5$ and 9.4 AU, for $N = 400$. Right: same labeling for charge neutrality at the midplane, for variable number of monomers N .





$\log(\Lambda)$ for $f_{\text{dg}}=1.e-D4$, HCO^+

